A&A 652, A52 (2021)
https://doi.org/10.1051/0004-6361/202140497
© ESO 2021

Astronomy & Astrophysics

Mapping a duck: geological features and region definitions on comet 67P/Churyumov-Gerasimenko

M. Leon-Dasi[1], S. Besse[2], B. Grieger[2], and M. Küppers[1]

[1] European Space Agency (ESA), European Space Astronomy Centre (ESAC), Camino Bajo del Castillo s/n, 28692 Villanueva de la Cañada, Madrid, Spain
[2] Aurora Technology B.V. for the European Space Agency (ESA), European Space Astronomy Centre (ESAC), Camino Bajo del Castillo s/n, 28692 Villanueva de la Cañada, Madrid, Spain
e-mail: sbesse@esa.int

Received 4 February 2021 / Accepted 12 May 2021

ABSTRACT

The data from the Rosetta mission have permitted a reconstruction of the shape of comet 67P/Churyumov-Gerasimenko and an identification of the terrains and features forming the surface. The peculiar shape of the comet has made it challenging to project these geological features onto an unambiguous frame. As a result, the geological maps published to date are created on top of comet images, making them dependent on the viewing angle and image resolution. To overcome this limitation, we present an integrated set of geological maps of the northern hemisphere of the comet, displayed in an unambiguous projection. The new maps combine the geological landmarks published in previous studies in a single framework and are completed with newly identified features. We have located the landmarks on OSIRIS images projected onto the surface of a three-dimensional shape model of the comet. For each region, the geological maps are displayed in the Quincuncial adaptive closed Kohonen (QuACK) map projection. The QuACK map solves the spatial ambiguity issues and reduces the shape and area distortions of classical global projections, which particularly affect the polar regions. The outcome of this research is a set of individual geological maps that are displayed both on top of OSIRIS images and in the QuACK map projection. These maps are analysed and grouped by similarities in terrain and morphology to find common characteristics that allow expanding our knowledge of the formation processes of comets. Based on this analysis, the north-south dichotomy is confirmed, and a redefinition of the regional boundaries is proposed for the Anubis-Atum and Aker-Babi frontiers. This research fills the gap in the field of mapping comet 67P/Churyumov-Gerasimenko and provides an innovative method for treating the surface of highly irregular bodies.

Key words. comets: general – comets: individual: 67P – methods: data analysis

1. Introduction

When the Rosetta spacecraft encountered comet 67P/Churyumov-Gerasimenko (hereafter 67P), one of its findings was the highly irregular and concave shape of the comet (Preusker et al. 2015). Cometary nucleus observations by spacecraft have revealed important morphology differences and globally two general families of nucleus shapes. The first category corresponds to comets 1P/Halley (Keller et al. 1986), 81P/Wild 2 (Brownlee et al. 2004), and 9P/Tempel 1 (A'Hearn et al. 2005), for which the size and volume can be approximated by a sphere. Although 1P/Halley is slightly elongated (Sagdeev et al. 1986), the distance at which the observations were taken is too far to properly evaluate the possible complex shape. In the second category, comets 19P/Borelly (Soderblom et al. 2002), 103P/Hartley 2 (A'Hearn et al. 2011), and 67P (Sierks et al. 2015) exhibit more elongated shapes that are often referred to as bilobate. The morphologies of the second category complicate shape reconstruction techniques in general, but 67P is quite particular. Because of the extremely irregular shape, there are overhang areas where different points on the surface have the same longitude and latitude (Grieger 2019).

Common global map projections such as the equidistant cylindrical projection (employed, e.g., by Vincent et al. 2016) cannot display the complete surface of 67P. In the naive application of these projections, some areas are missing and boundaries appear between regions that are not connected in reality. Additionally, the regions close to the poles are extremely distorted, just as for spherical bodies such as the Earth. Therefore it has been difficult to project the shape of 67P onto a single two-dimensional map. When surface properties or features are mapped, the following solutions have been tried. The most common approach has been to directly map features onto images (Pajola et al. 2015; Giacomini et al. 2016). This allows a quick estimate of the position of a feature, but the accuracy is limited due to projection effects and illumination conditions. Another significant disadvantage of this approach is the dependence of the mapping on the image itself. The identification of similar features on other images has to be done manually, which is a time-consuming task prone to errors. Preusker et al. (2015) proposed to map the two lobes of the bilobed comet nucleus separately, with a third map for the so-called neck that connects the two lobes. The individual parts of the nucleus are indeed better approximated than by common map projections, but the boundary regions between them are difficult to represent in this scheme. A third approach is mapping directly on the three-dimensional shape model (Thomas et al. 2018). This provides an adequate representation of individual regions and geological landmarks, but several three-dimensional representations are needed to show the full nucleus.

Geological units and landmarks of 67P have been mapped by numerous authors (El-Maarry et al. 2015, 2016, 2017;

Giacomini et al. 2016; Pajola et al. 2015; Birch et al. 2017; Thomas et al. 2018; Auger et al. 2015) following different methods and objectives. Furthermore, different geological terminology has been used within these publications to describe similar features and processes. All of this often complicates a cross-analysis of these publications. In order to solve these problems, we present all geological features in a common framework, making use of the Quincuncial adaptive closed Kohonen (QuACK) map (Grieger 2019). This is an extended version of the Kohonen map (Kohonen 1982), a self-organising neural network that can be used to assign unique two-dimensional coordinates to each point on the surface of a three-dimensional body.

In Sect. 2, we describe the types of features we considered in the map and the mapping procedure. In Sect. 3, we present two-dimensional representations of the regions defined on the surface of 67P with the QuACK unambiguous projection and discuss the types of boundaries that form these regions. Section 4 is dedicated to regional maps of the surface features and their projection in a two-dimensional framework that can be used with any image of the comet 67P. In Sect. 5, we discuss the findings on comet morphology based on our new approach, and we also propose some minor changes to the region definitions. Section 6 finally summarises our conclusion on this mapping of the northern hemisphere of 67P.

2. Mapping philosophy, data products and tools

2.1. Images and shape model

The geological mapping of comet 67P has been done using the Small Body Mapping Tool (SBMT, Ernst et al. 2018), a very efficient software for mapping small bodies. It has successfully been used to map other targets of the Rosetta mission (Besse et al. 2014). This tool allows visualising and editing the products of the OSIRIS camera on board the Rosetta mission (Keller et al. 2007) onto a three-dimensional shape model of the comet. Moreover, the tool provides the option of outlining five types of structures (paths, polygons, circles, ellipses, and points) on the mesh of the body. The combination of these two capabilities is exploited to create geological maps directly on images projected onto the surface of a three-dimensional model of comet 67P. In this particular case, images from the OSIRIS narrow-angle camera (NAC) projected onto the surface of the DLR SHAP4S model (Preusker et al. 2015) were used for the mapping. Figure 1 displays the comet morphology and an example of the image projection onto the surface. To properly constrain the mapping, a total of 66 images with different target locations, illumination conditions, and viewing angles were used; see Table A.1. The selected images were acquired between August and September 2014 at an altitude range from 29 to 116 km, resulting in a spatial resolution ranging from 0.5 to 2.2 m/pixel. The images correspond to the MTP007 (European Space Agency, 2019-01-31, RO-C-OSINAC-3-PRL-67PCHURYUMOV-M07, V3.0.[1]) and MTP008 (European Space Agency, 2019-01-31, RO-C-OSINAC-3-PRL-67PCHURYUMOV-M08, V3.0.[2]) periods and are available at the Planetary Science Archive (Besse et al. 2018). Because only a limited number of images are available on the SBMT, only the northern hemisphere was mapped, which corresponds to 17 of the 26 regions of 67P: Aker, Anubis, Anuket, Apis, Ash, Aten, Atum, Babi, Hapi, Hathor, Hatmehit, Imhotep, Khepry, Ma'at, Nut, Serqet, and Seth, as defined in El-Maarry et al. (2017).

[1] https://doi.org/10.5270/esa-y6dezqw
[2] https://doi.org/10.5270/esa-18oml01

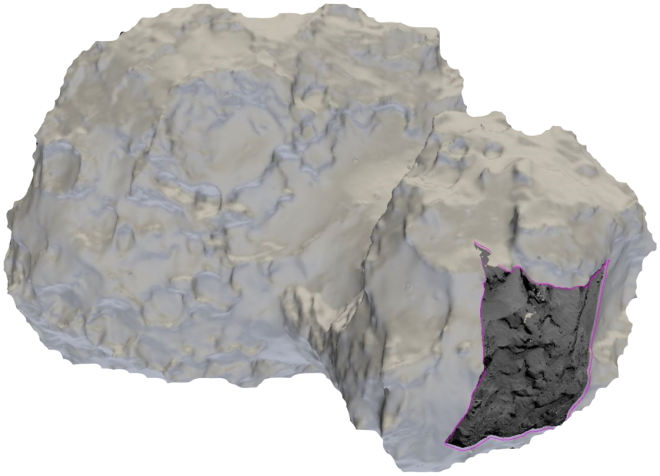

Fig. 1. View of the DLR SHAP4S shape model of comet 67P on the SBMT with a projected image from the OSIRIS NAC camera.

The global and regional map projections presented in Sects. 3 and 4.2 follow the regional unit definition established by Thomas et al. (2018) on the surface of the SHAP7 shape model, with a resolution of 0.2 million facets. It is noted that different shape models are used for the geological mapping and the region definition, respectively. The SHAP4S model covers 70% of the comet surface and accurately describes the northern hemisphere, while the SHAP7 extends the accurate coverage to the complete surface (Preusker et al. 2017). Being focused on the northern hemisphere, the inaccuracies derived from the usage of different shape models remain minimal and do not affect the results of this work.

2.2. QuACK

On the SBMT, the features are mapped in the Cheops reference frame (Preusker et al. 2015), hereafter referred to as "original coordinate system". To create geological maps of such an irregular body, the features are transformed to the QuACK map and are either directly displayed therein or are further transformed using generalised coordinates.

The QuACK projection (Grieger 2019) maps the complete surface of 67P to a square. It is topologically equivalent to the Peirce quincuncial projection of the world (Peirce 1879; Grieger 2020), which maps the global sphere to a square. This enables assigning generalised longitude and latitude to each point of the surface of 67P that is unambiguous, see Fig. 2. Red and green lines are the original coordinates. If we follow the 0° longitude starting from the north pole near the centre in upward direction, we find it crossing the 30° latitude three times. This confirms that there are multiple points with the same longitude and latitude. This holds for all the points in this overhung area and many others at smaller scales (Grieger 2019). White and black lines are the generalised longitudes and latitudes that we assigned to the surface points of 67P. These correspond to a traverse aspect of the quincuncial projection and are clearly unambiguous. We can use these generalised coordinates to apply any map projection such as the equidistant cylindrical in an unambiguous way, displaying the complete surface.

We note that north and south pole of the generalised coordinates are close to the original ones, but they do not match exactly. They almost match because of the rotation dynamics of 67P, which determines the pole locations, as described by Grieger (2019). While the deviation of the pole locations is small, in

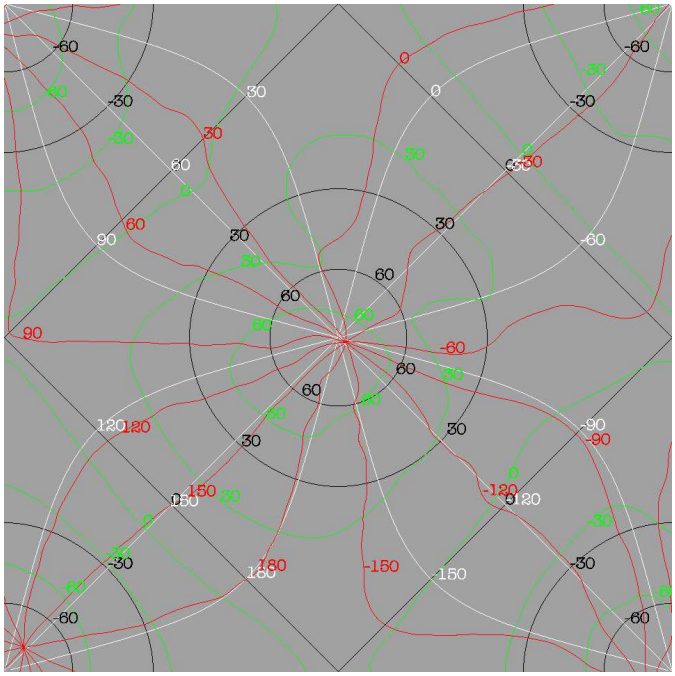

Fig. 2. QuACK map projection with longitudes and latitudes. Red and green: original longitudes and latitudes, respectively, as directly computed from the three-dimensional surface points of 67P. White and black: generalised longitudes and latitudes, respectively, assigned to each surface point via the QuACK map.

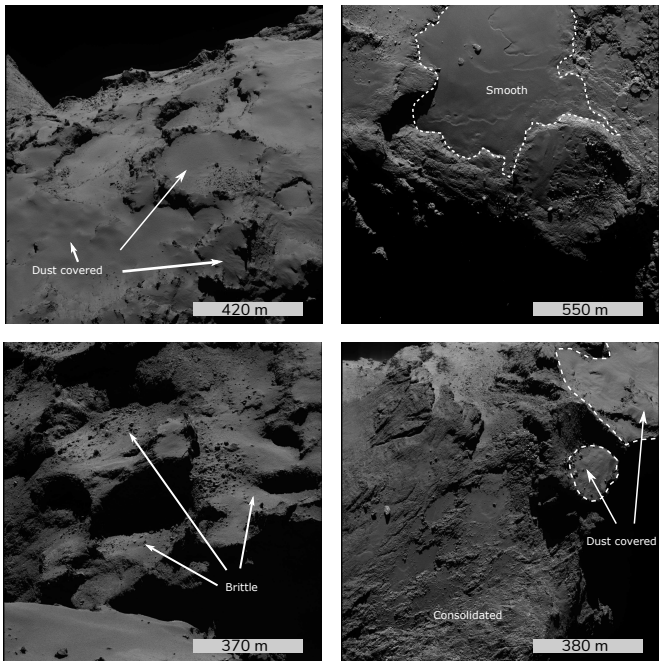

Fig. 3. Example of terrain types. *Top left*: dust-covered terrain in the Ash region. *Top right*: smooth terrain in the Imhotep region. *Bottom left*: brittle terrain in the Seth region. *Bottom right*: consolidated terrain in the Aker region and dust-covered terrain in the Babi region.

the case of the south pole, they reside in different regions. This yields large differences in the region shapes in the generalised version of the equidistant cylindrical projection, because of the large distortion that this projection introduces in the polar areas.

The QuACK map is not defined by a simple analytic transformation, but by a special shape model that can be unfolded into a two-dimensional map. In order to facilitate the application of the QuACK map projection, software is available on GitHub[3]. Among Fortran subroutines and shape model data, the ∗nix style command-line tool quack is provided. This was used to create the QuACK maps shown herein.

2.3. Geological features

Five types of large-scale terrain types were considered following the classification from Thomas et al. (2015): strongly consolidated, smooth, brittle, large-scale depressions, and dust-covered terrains. Although this classification does not follow a single criterion it is useful to associate morphological features with the underlying type of terrain. A region can present multiple types of terrain, as analysed by Thomas et al. (2018). In this work, the dominant terrain for each region is considered. Figure 3 illustrates the consolidated, smooth, brittle, and dust-covered terrains. The classification is defined as follows:

Strongly consolidated. Terrain with a rocky appearance that can present morphological features such as ridges, outcrops and linear fractures and shows no signs of collapse.

Smooth. Flat surface that does not show impacts or underlying structures. It is found enclosed by consolidated material and can be covered with boulders.

Brittle. Terrain showing multiple evidence of collapse and fractures that result in niches or small-scale depressions covered with boulders.

Depression. Large-scale areas of at least 1 km length along the principal axis at lower elevation than the surroundings. The depression can present any shape and can contain internal morphological features.

Dust covered. Surface covered with dust, with a coating that is thin enough to identify underlying structures such as craters, niches, or fractures (e.g. below the dust-covered regions of Ash and Ma'at, a brittle terrain is visible).

For the geological maps, we classified the surface features into ten types: six linear and four circular types. A summary of these geological features is presented in Table 1 and is illustrated in Figs. 4 and 5.

2.3.1. Linear features

The linear features are classified into six categories: terraces, scarps, pits and niches, ridges, rims, and fractures. The categories are defined as follows.

Terraces. Defined as flat surfaces bounded by a steep descending slope. The terrace is mapped as the line forming the boundary between the plain and the descending slope, also called the terrace margin. For this mapping, the terraces considered have a minimum length of 20 m.

Scarps. When the descending slope forms an angle close to 90° with the terrace plain, it forms a wall and the base is classified as a scarp. This feature is mapped by the contact of the vertical wall with the ground. The scarps considered have a minimum length of 20 m and a minimum height of 10 m. Not every terrace has a corresponding scarp, since the descending slope

[3] https://github.com/esaSPICEservice/QuACK

Table 1. Feature-mapping criteria.

Feature	Mapping criterion	Min. size	Map
	Linear features		
Terrace	Terrace margin	20 m	
Niche	Top of the feature	20 m	
Ridge	Upper edge	100 m	
Rim	Upper edge	100 m	
Fracture	Along the feature	15 m	
Scarp	Contact with lower plain	20 m	
	Circular features		
Boulder	Enclose the feature	∅5 m	
Mound	Enclose the feature	∅5 m	
Crater	Enclose the feature	∅5 m	
Bright patch	Enclose the feature	∅2 m	

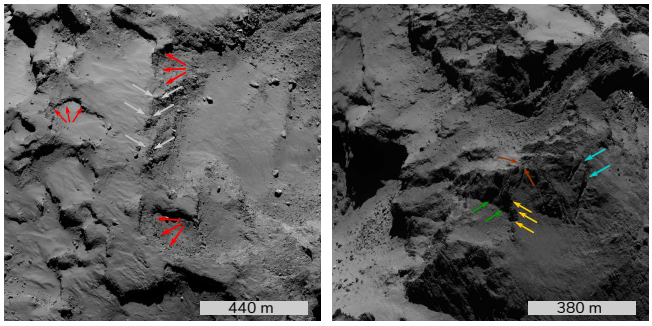

Fig. 4. Example of linear features. *Left*: depression rim (grey), and niches (red) in the Hatmehit region. *Right*: fractures (blue), ridge (brown), terrace (yellow), and scarp (green) in the Aker region.

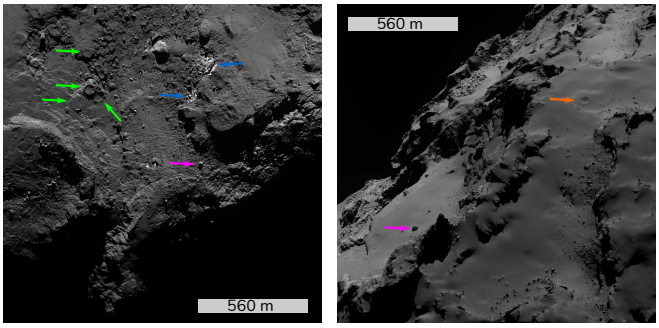

Fig. 5. Example of circular features. *Left*: circular mounds (green), bright patches (blue), and boulder (pink) in the Imhotep region. *Right*: boulder (pink) and impact crater (orange) in the Ash region.

bounding the plain can be gradual or too short to be mapped. In the geological map, the distance between a terrace and its corresponding scarp can give a reference to the slope and the height of the latter.

Pits and niches. Similar to the terraces, circular depressions forming pits or niches are of significant importance in the understanding of the activity and evolution of the comet (Vincent et al. 2015). For this mapping, pits are cylindrical holes on the ground, while niches are defined as semi-circular walls that appear to be remnants of circular pits (Lee et al. 2017). As in the case of the terraces, niches are mapped by the boundary between the upper terrain and the descending slope, and therefore take the shape of a convex segment. The niches can also be bounded by a scarp.

Ridges. Comet 67P shows some landmarks with a mountain range appearance, which are mapped as a ridge. This feature is defined as the boundary connecting two ascending slopes. These slopes are named hillsides and can be steep or gradual. The end of a ridge is marked by either the encounter of the mountain crest with the ground or by the encounter with a wall perpendicular to it.

Rims. El-Maarry et al. (2015) has defined three regions as large-scale depressions. The edge of these regions is usually elevated with respect to the surroundings and is mapped as a depression rim. Note that since the rim is a definition of the perimeter of the depression, this feature can be overlapped with other types of linear features such as niches or terraces.

Fractures. Defined as linear cracks on the surface which can be identified though the view of the crack wall or through a darkening formed by the crack inner shadow. This feature is mapped at a minimum length of 15 m.

2.3.2. Circular features

The circular features are classified into four categories: boulders, circular mounds, impact craters, and bright patches. The categories are defined as follows.

Boulders. This constitutes the dominant circular feature. Pajola et al. (2015) identified more than 3,500 boulders larger than 7 m in diameter. For this mapping, boulders were defined as large rocks that can be distinguished individually and have a minimum size of 5 m in diameter. Boulders can be found isolated or clustered.

Circular mounds. This category is defined to map a particular type of feature that is only found in the Imhotep region. It corresponds to the roundish features mapped by Auger et al. (2015). These are circular or elliptical plateaus, elevated with respect to the surrounding and bordered by a rim.

Impact craters. Impact craters are also specifically defined for a singular case because only one possible impact crater has been found on the surface. It is located in the Ash region (El-Maarry et al. 2015). It was mapped as an ellipse matching the crater rim.

Bright patches. The patches are defined as a roundish feature with a higher albedo than the surroundings. From this analysis, the source and composition of these bright patches cannot be determined. The size threshold was lowered to 2 m in diameter because of the characteristic dimension of this feature. These features were therefore identified using high-resolution images in which the diameter is covered by at least three pixels.

3. Regional unit definition in 2D projection

To introduce a regional map of the comet that fully represents the boundaries between the regions, we used four projections: the equidistant cylindrical with original coordinates presented in Fig. 6, the equidistant cylindrical with generalised coordinates in Fig. 7, and the QuACK projection, centred on north and south, in Figs. 8 and 9, respectively. All figures show the comet regions coloured according to the dominant type of terrain as defined by

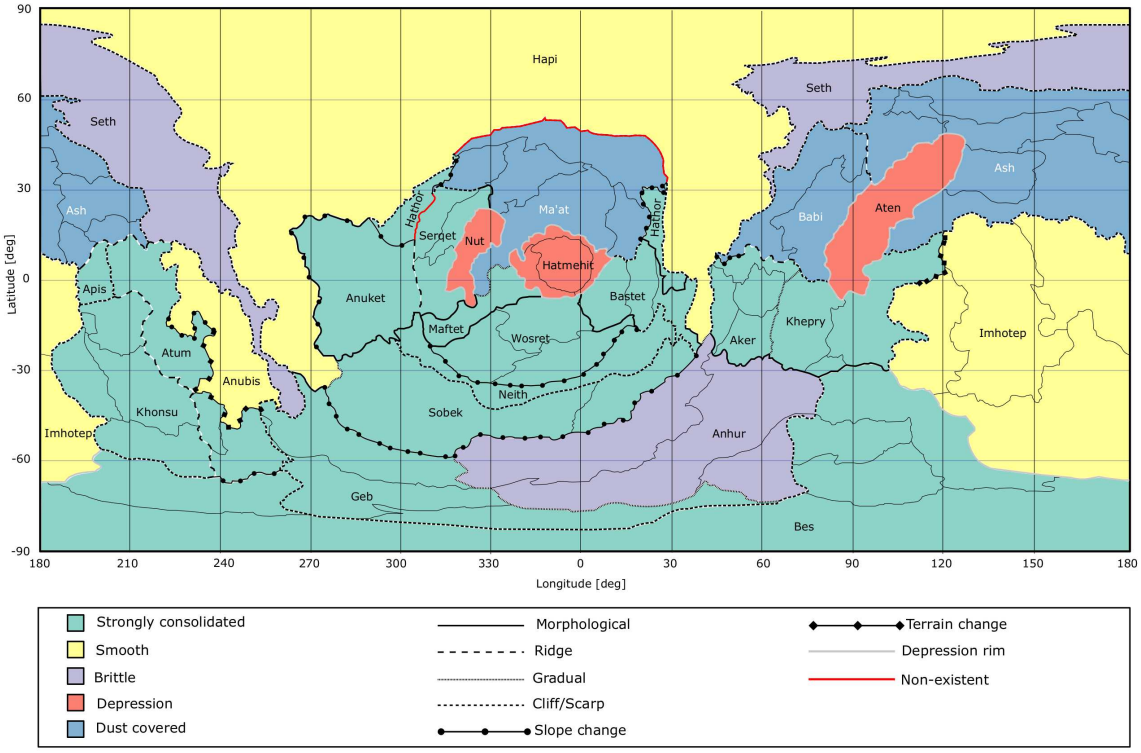

Fig. 6. Equidistant cylindrical projection of region terrains and boundaries of comet 67P. A portion of the Hathor region is not visible because of the overhangs. The subregion boundaries as defined by Thomas et al. (2018) are also represented.

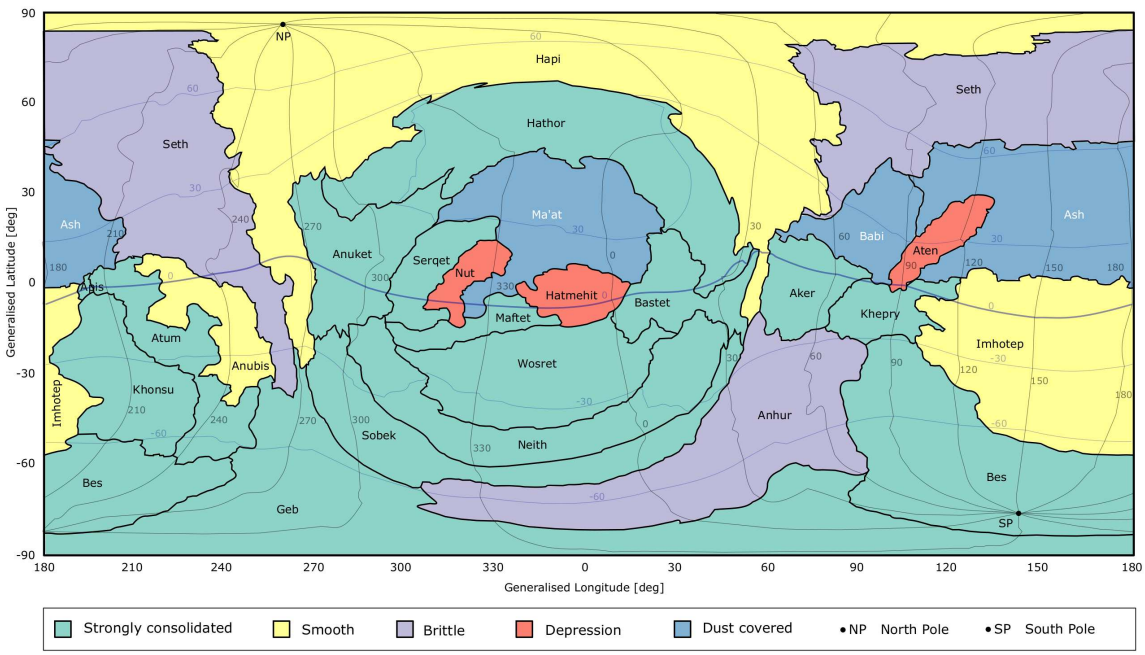

Fig. 7. QuACK equidistant cylindrical projection of region terrains of comet 67P. Purple: original latitude. Grey: original longitude.

El-Maarry et al. (2015, 2016). In this section, the regional boundaries correspond to the definition by Thomas et al. (2018). In Sect. 5 we propose two modifications based on the interpretation of the geological mapping.

The global map in equidistant cylindrical projection with the original coordinates is presented in Fig. 6. The projection has been used in previous research to map the comet terrains (Birch et al. 2017), to pinpoint the location of features such as jets (Fornasier et al. 2019; Lara et al. 2015; Schmitt et al. 2017) and bright patches (Deshapriya et al. 2018) and to display the measurements of Rosetta instruments (Filacchione et al. 2019). To connect with these studies, we selected the equidistant cylindrical projection as a baseline to indicate the types of regional boundaries and the extent of the subregions. Although this layout is familiar, it fails to correctly represent the contact between regions due to the coordinate overlap which especially affect the

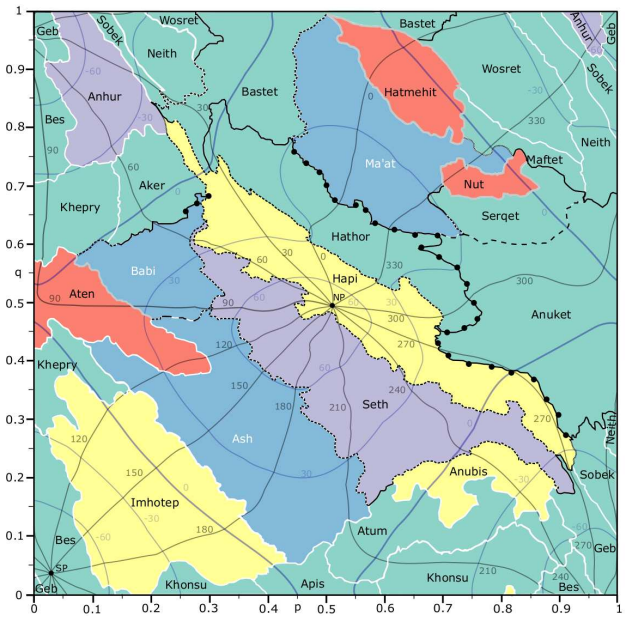

Fig. 8. North-centred QuACK projection. Black boundaries indicate the border type of the regions with longitude or latitude ambiguities. The original coordinate grid is represented on top. Purple: original latitude. Grey: original longitude. Colours and line styles correspond to the legend in Fig. 6. Axis annotations show the QuACK map coordinates p and q.

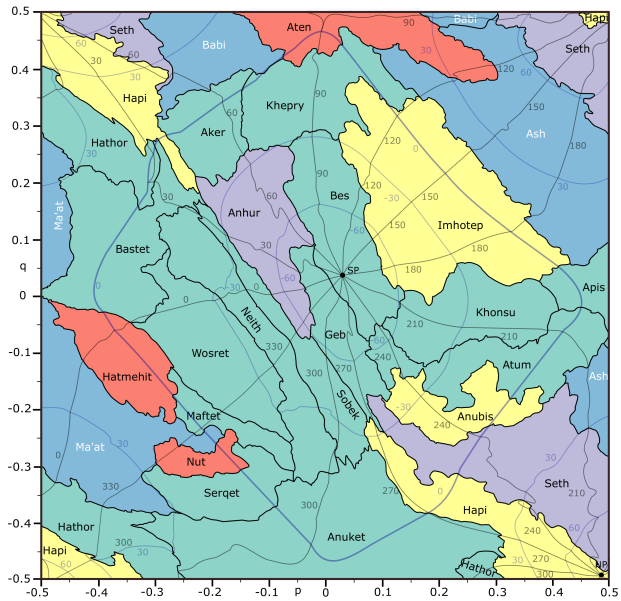

Fig. 9. South-centred QuACK projection. Original coordinate grid represented on top. Purple: original latitude. Grey: original longitude. Colours correspond to the legend in Fig. 6. Axes annotations show the QuACK map coordinates p and q.

central area of the map. For a given representation, some areas of the comet are thus hidden, and therefore the displayed boundaries are incorrect. This effect is represented by the red lines in Fig. 6 and is particularly applicable to the Hathor region.

To solve this ambiguity, we used the generalised longitudes and latitudes introduced by the QuACK projection, cf. Sect. 2.2. To understand the transition to the QuACK layout, we first introduce the equidistant cylindrical projection with generalised coordinates in Fig. 7. The original coordinate grid is represented on top of the map to make the link with the generalised coordinates. This set of generalised coordinates is merely a tool to represent the complete surface of the comet unambiguously, and it is not aligned with the original set of coordinates. This explains that the south pole, which is located in the Bes region appears in Geb with the generalised coordinates. When the two maps are compared in equidistant cylindrical coordinates, we confirm that the central region suffered the largest ambiguity. The Hathor region, in which a cliff joins the small lobe with the neck, was almost completely unexposed with the original coordinates, creating the incorrect Hapi-Ma'at boundary that does not exist in reality. With the QuACK equidistant cylindrical projection, the real boundaries are displayed, and it is easier to understand the transition from the small to the big lobe. Figure 7 allows visualising the coordinate overlap through the double crossing of longitude-latitude lines, for example over the Hathor and Ma'at regions. However, this projection still has the problem of presenting large distortions in the polar areas. As a result, the Hapi, Seth, Geb and Bes regions appear to be larger and more elongated than they are in reality. This projection is therefore not optimal to produce individual geological maps of each region on the comet because the features located in these areas would be highly distorted.

The QuACK map was used to produce an unambiguous projection of the comet that minimises the distortions. Figure 8 shows the north-centred QuACK projection with the original coordinate grid. The regions that showed coordinate ambiguities are highlighted with black borders to add the types of boundaries that could not be mapped in Fig. 6. In this map, the north pole is approximately in the centre of the square, and the south polar area is wrapped around the four corners. This explains the multiple appearance of the Geb and Bes regions. It is again useful to visualise the coordinate overlap. If the comet were a sphere, the 30-degree latitude line would be circular. In this case, the line forms an eight-shape as a result of the overhang in the small lobe. The portion that deviates from the circle results in coordinate overlaps. The main advantage of this map is that it reduces the distortion around the poles. This allows creating geological maps that are closer to the real shape of the regions (with a few exceptions to discuss). When the south pole is approached, some of the regions are divided and appear on different sides of the square. This can at first constitute a problem when the comet is visualised projected in this layout. To avoid this issue, the south-centred QuACK projection is presented in Fig. 9. It can be constructed by tessellating four instances of the north-centred QuACK map (two of them are upside down) and then cropping around the centre, where four corners match, cf. Grieger (2019).

In the south-centred projection, the south pole is approximately at the centre and the north pole is wrapped around the four corners. The latitude lines are closer to forming a circle, which verifies that the coordinate ambiguity is smaller in the southern hemisphere. The regions that were divided in the northern view appear unified in this view. With the QuACK map in the north- and south-centred projection, the ambiguity and the distortion issues are solved. Therefore this projection is best suited for creating most of the geological maps. However, this projection is deformed at the centre of the square edges (a "feature" inherited from the topologically equivalent Peirce quincuncial projection, Peirce 1879).

At these four critical points, approximate conformality breaks down. To illustrate what happens there, imagine a hand fan that is completely unfolded to 360° with some shape painted on it. Now we evenly fold it back to 180°. This is what happens to

a region that encompasses one of these critical points: the region is turned inside out. This drastic distortion affects the regions of Apis, Anuket, Bastet, and Aten. We did not map Bastet here. For the other three regions, the geological maps introduced in Sect. 4.2 are projected using the QuACK equidistant cylindrical layout from Fig. 7 in generalised coordinates.

The combination of Figs. 7 and 8 provides a complete description of the comet regions and how they interact. The types of boundary between regions were derived from the analysis of El-Maarry et al. (2015, 2016) and were slightly revised to match the geological mapping performed in this work. Seven types of boundaries are considered. Ridges, scarps, and depressions match the description provided in Sect. 2.3.1. When the boundary is formed by a sloping terrain, that is not steep enough to form a scarp, it was mapped as a slope change. A terrain change refers to an abrupt encounter between two types of the terrain types defined by Thomas et al. (2015). This boundary type is found in two occasions, at the border between consolidated and smooth areas. When the encounter between types of terrains or surface morphologies is smooth, it was categorised as a gradual boundary. Finally, the morphological boundary was used by El-Maarry et al. (2015) to characterise changes in the surface that did not fit in the other categories. We tried to improve this definition, and for the northern hemisphere, we reclassified the morphological boundaries into one of the other six categories. We were unable to do this in the southern hemisphere, where the morphological boundaries were kept.

Some borders are defined by more than one type of boundary. This is the case of the Ash-Babi frontier, which starts with a scarp, develops into a ridge and ends with a second scarp. In some cases, the existence of different boundary types within one frontier indicates that the definition of this border is not clear. This is the case of the Anubis-Atum frontier. The boundary starts with a scarp that softens to a slope change, and finally, it is defined by the transition from a smooth terrain in Anubis into a consolidated terrain in Atum. The same type of boundary is found between Imhotep and Khepry, where it starts as a scarp and develops into a terrain change from smooth in Imhotep into consolidated in Khepry.

4. Regional mapping

Following the mapping criteria described in Sect. 2.3, we developed individual maps for the regions covering the northern hemisphere of comet 67P. Section 4.1 presents the maps that we created with the SBMT software with the OSIRIS NAC images directly projected onto the comet surface. Section 4.2 presents the geological maps of each region with its corresponding subregions. The north-centred QuACK layout is used to project these maps, except for Khepry and Imhotep, for which we used the south-centred QuACK layout, and the regions of Aten, Anuket, and Apis, for which we use the equidistant cylindrical map in generalised coordinates. For the regions projected in QuACK layout, the axes provide map coordinates p and q corresponding to Figs. 8 and 9.

4.1. Maps on OSIRIS images

The circular and linear features were identified using a combination of high-resolution images that were especially selected for each region. The use of several images projected onto a three-dimensional shape is very helpful to understand the depth and effect of shadows on the surface. In this way, we avoided misinterpreting features because images were used that depend on illumination. The drawback of using multiple images to map a single region is that the different viewing angle may cause the features to appear shifted from one image to the other, which complicates the task of representing everything in a single figure. The motivation for including these figures is that we wished to show a physical depiction of the mapped features, which will help describe and understand the geological maps presented in Sect. 4.2.

The maps on top of OSIRIS images were also included to relate the features to maps presented in other publications and understand how they differ from or complement this work. The geological mapping conducted by Giacomini et al. (2016) of the northern hemisphere was used as a baseline for this mapping, but the two approaches are substantially different. Giacomini et al. (2016) defined four types of linear features: fractures, cuesta ridges/terrace margins, niches, and strata. To understand the relation of the two mapping approaches, we note that there are two categories, rims and scarps, that are only defined in our mapping, but we do not include strata. Fractures follow the same definition in both mappings. Moreover, we distinguished between terraces and ridges. While niches are defined in a similar way in both approaches, the distinction between terrace and niche is subjective. In the map of Giacomini et al. (2016), the images were acquired at an altitude range of 64–130 km, while the images selected for this work are at an average altitude of 40 km. This allows us to focus individually on each region and map smaller features. As a reference for the map, we also followed the description of El-Maarry et al. (2015) of the regional surface morphology. It is useful to understand how his classification is adapted to the criteria followed by our work. This analysis does not include geological units, and thus the classification of smooth deposits, dust/airfall, or collapsing material does not apply here. For the linear features, terraces, fractures, ridges, rims, and scarps follow the same criteria as were applied in this work. El-Maarry et al. (2015) also considered layering and lineaments which in this work are classified as either terraces or niches. For the circular features, boulders and craters are defined similarly. Finally, the detailed geological mapping of Imhotep performed by Auger et al. (2015) was used as a baseline to map this region. In this work, the linear features are grouped into one category and the circular features are classified into boulders and roundish features. Roundish features correspond to pancake-shaped mounds in the nomenclature of El-Maarry et al. (2015) and circular mounds in our classification. We note that we did not map the linear features in the smooth plain of Imhotep because they undergo temporal changes (Groussin et al. 2015) and do not correspond to the classification of terraces adopted here.

Only images from August to September 2014 were used, which cover the Northern hemisphere at the highest resolution. Therefore this analysis does not cover the temporal changes on the surface of the comet. Features that are known to vary in the course of the comet orbit such as honeycomb structures and short receding scarps (El-Maarry et al. 2017), cliff collapse (Vincent et al. 2016), and bouncing boulders (Vincent et al. 2019), were not included.

Because we used multiple OSIRIS images, they overlap and it is difficult to display the mapping performed in one single figure. As a result, some of the features we mapped are concealed in a background view. This is the case of the Hapi region in Fig. B.7, where a fracture of 400 m is mapped, but only the beginning can be observed with this particular image because then it enters a shadowed region.

The complete set of features identified in OSIRIS images can be found in Appendix B. As an example, features identified in

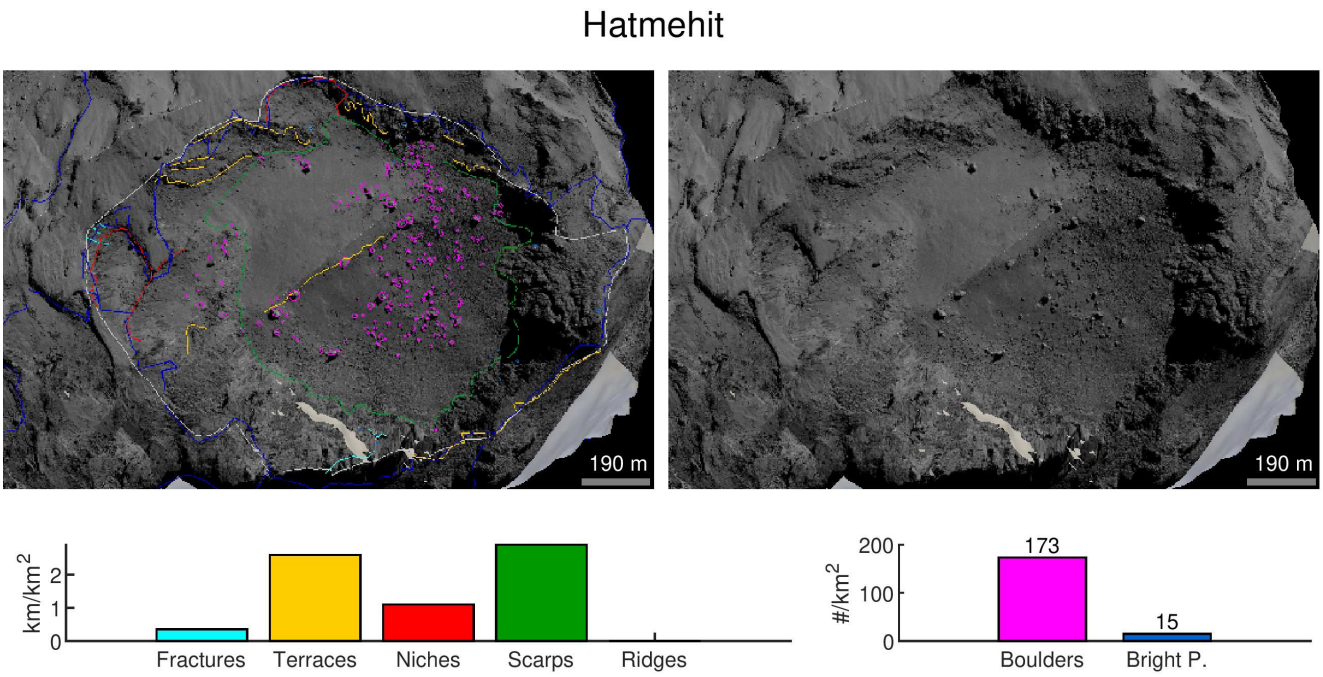

Fig. 10. Identification of features in the Hatmehit region from images projected onto the SHAP4S shape model and annotated on the SBMT.

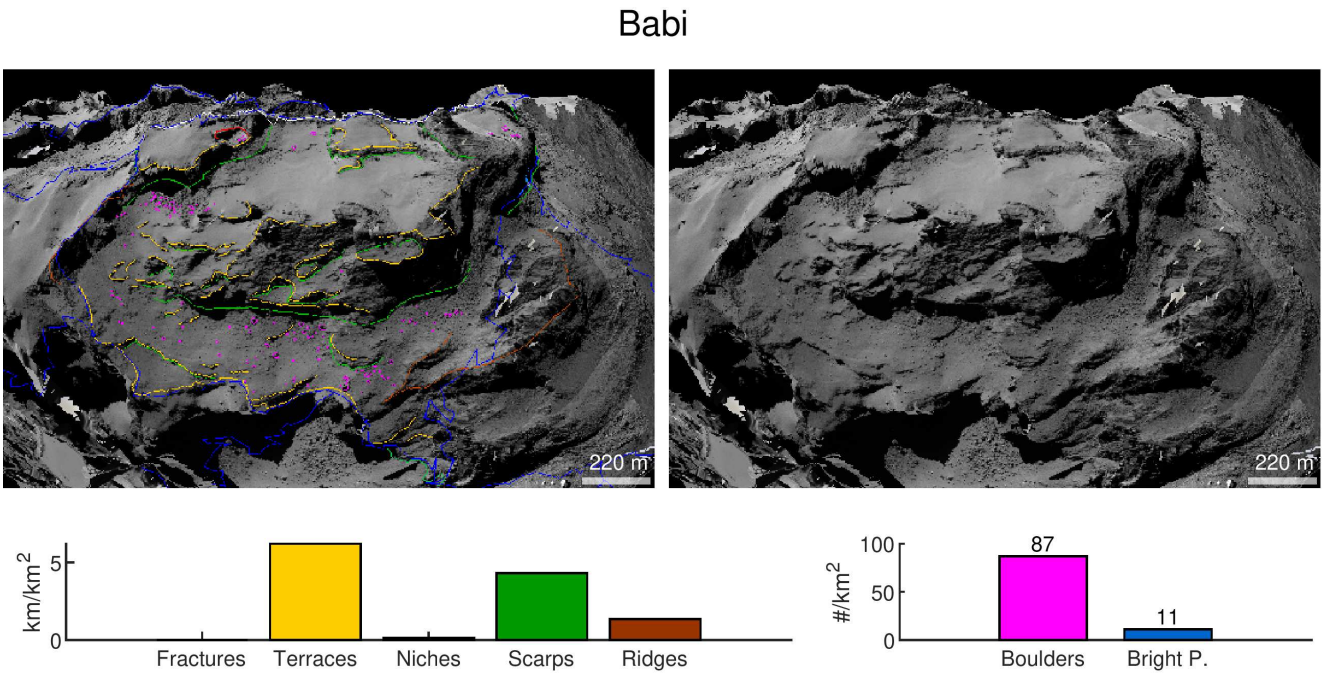

Fig. 11. Identification of features in the Babi region from images projected onto the SHAP4S shape model and annotated on the SBMT.

the Hatmehit and Babi regions (Figs. 10 and 11) are included in this section. For each region, two images are presented. The first contains a blue line delimiting the extent of the region and the features we mapped following the criteria from Table 1. The blue line is based on the region definition by Thomas et al. (2015), which was originally mapped in the SHAP7 model, and is displayed here on the SHAP4S. The second image is a plain view of the surface, used to clearly visualise the features that we mapped on top. Two statistics are shown, one for the linear features and one for the circular. Rims, craters, and circular mounds are not included in the statistics because they constitute specific cases applicable only to a few regions. The upper bar plot contains a measure of the added length of features of one type divided by units of area in the region, and are expressed in km km^{-2}. Boulders and bright patches are measured by the total number of each feature in a region divided by the region area.

4.1.1. Terraces

Terraces are defined as a flat surface bounded by a slope. This definition encompasses a series of cases depending on the size, height, and location of the feature.

A first category includes the terraces that are located on descending slopes, usually comprised by several terraces resting

on top of each other. They can be found in depression rims, such as in Hatmehit and Aten, or in inclined regions such as Anuket and Babi, see Figs. 10, B.1, B.2, and 11. These terraces are usually short and are followed by a small scarp. They are found in consolidated terrains.

Terraces in planar consolidated regions such as Apis, see Fig. B.3, constitute a second category. In this case, all terraces are aligned in the same direction and are slightly curved. In the smooth areas of Imhotep and Anubis, and in the centre of the Hatmehit depression, see Figs. B.4, B.5, and 10 a special type of terraces is found. These terraces are less pronounced than those in the more consolidated regions, and in the case of Imhotep and Anubis, they present multiple curves in a zigzagging shape. In these terraces, the transition from the plain to the underneath surface is so smooth that the scarp cannot be clearly differentiated.

Finally, this feature is found in areas with abundant erosion in the form of niches, such as Atum, Seth, and Ma'at, see Figs. B.6, B.8, and B.9. These regions contain many terraces that connect the niches. These terraces are usually longer than in the other categories, and are sufficiently deep to be bounded by a scarp.

4.1.2. Niches

Niches are defined as the remnants of circular pits, resembling a semi-circular depression and exposing layers of the comet. Niches can be classified according to their position and orientation, without entering into geological interpretations of their origin and evolution (for further interpretation of the niches see Besse et al. 2015).

It is common to find niches located in the rim of depressions. As explained in Sect. 2.3, a rim is defined as the feature constraining the extent of a depression and can be overlapped with other features. In the regions of Hatmehit and Nut, the depression rim is caved with a semi-circular shape mapped as a niche (Figs. 10 and B.10). A similar example is found at the boundary between Khepry and the lower lying Imhotep, see Fig. B.4. This type of niche carves all the way from the top to the bottom of the rim, and its size is proportional to the size of the depression.

A second category corresponds to isolated niches with no apparent preferential direction. These features appear in the dust-covered regions of Ash and Ma'at, see Figs. B.11 and B.9. These niches are found in several directions and appear smoothed by the dust coverage. The Ma'at region contains nine niches, scattered along the region and facing in all directions. The case of Ash is more complex, since the region revolves around the comet. It contains close to twenty niches facing multiple directions.

In the case of the niche-covered Seth region, the niches are oriented in a single direction. see Fig. B.8. In this case, all the niches are facing towards the Hathor cliff and are located consecutively, revealing the layering of the comet's interior. These features have provided a greater understanding of the interior structure of 67P and have allowed to develop models of the formation (Massironi et al. 2015) and the layered structure of the comet (Penasa et al. 2017). In many of these niches we find an accumulation of boulders, a characteristic that was not found in the other types of niches.

4.1.3. Fractures

Fractures are identified as darker lines on the surface that reveal the inside of the comet. They are found in multiple appearances according to which we classified them into three categories. First, we note that most of the fractures are located on cliffs/scarps or steep slopes. Within these, two classifications are made: vertical and horizontal fractures.

Vertical fractures are usually found on cliffs or slopes. They are aligned with the gradient of the slope plane and are found in four regions: Hathor, Imhotep, Anubis, and Serqet (Figs. B.12, B.4, B.5, and B.13). In this category, we distinguish between the fractures in Hathor and in the other regions. The morphology of Hathor is unique in the comet, featuring dozens of deep fractures that are hundreds of meters long. This is not the case of Imhotep, Anubis, and Serqet. In these three regions, vertical fractures are found in scarps of approximately 100 m in height and have an average length of 60 m. These fractures are found in consolidated terrains and are grouped into clusters of five to ten units.

Second, we also find horizontal fractures on cliffs or slopes. They appear in the regions of Aker, Anuket, and Khepry (Figs. B.14, B.2, and B.15). In Anuket, where the slope is more gradual, these fractures are isolated and about 60 m long. Aker and Khepry contain multiple fractures that are hundreds of meters long. In Aker, a cluster of fractures is found at the side of the ridge with Babi, and another on the cliff descending towards Hapi. In both locations, the fractures are aligned and grouped, and can be clearly distinguished from images taken at an altitude of one hundred kilometres.

Finally, we find fractures in flat regions such as Apis, Atum, and Hapi (Figs. B.3, B.6, and B.7). In the cases of Apis and Atum we find multiple aligned fractures. In Apis, they are aligned with the terraces, but in Atum they do not present any apparent relation with the orientation of other features. Hapi contains a single large fracture that appears to widen in several locations instead of being a uniform crack (Giacomini et al. 2016).

4.1.4. Ridges

Regarding the ridges, there are fewer examples but the broad definition of the feature gives rise to multiple variations in morphology.

The smaller ridges that were identified have a length of 150–200 m and are located inside the depressions of Nut and Aten (see Figs. B.10 and B.1). These ridges are found near the rim of the depression and are characterised by a short altitude and a steep side, resulting in a narrow feature. Following in size, we find a set of ridges in the Atum and Anubis regions with very similar characteristics (see Figs. B.5 and B.6). These ridges are approximately 250 m in length, and unlike those in Nut and Aten, they present a very wide hillside and a less pronounced summit. Anubis and Aten are neighbouring regions, and these four ridges are oriented in the same direction. Similarly, but lying in more consolidated terrain we find the ridges of Apis, Khepry, and the centre of Aker (Figs. B.3, B.15, and B.14). These are well-defined ridges with fractures and boulders on the hillside, which is different from the previously described features.

Finally, we distinguish ridges that create strong morphological changes. In the map presented in Fig. 6, we observe that ridges can delimit regions and constitute a boundary between types of terrain and surface morphology. A clear example of this are the two ridges in Babi, which form the boundaries between this region and Ash (left) and Aker (right) in Fig. 11. The ridge with Aker marks the border between the fractured side in Aker to the terraced and boulder covered side in Babi. The ridge with Ash marks the transition from the dust-covered and even terrain in Ash to the less dust-covered and heavily bouldered terrain in Babi. Another ridge that defines a radical change in morphology

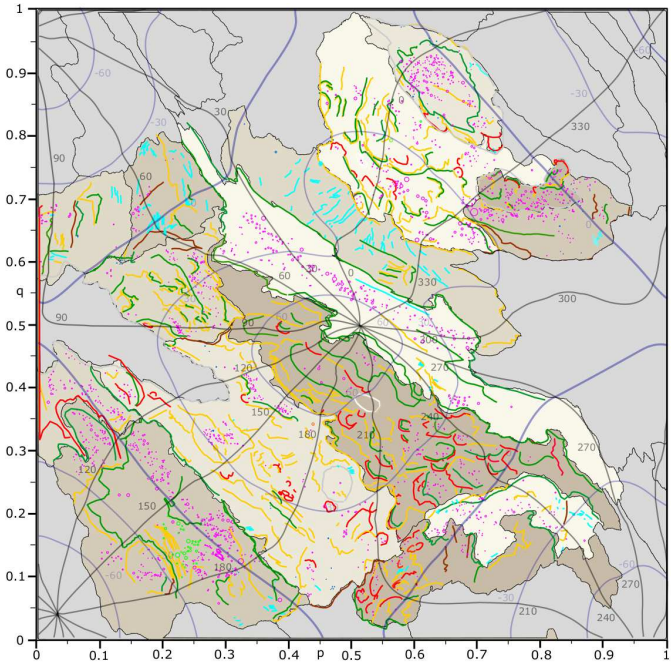

Fig. 12. Combined geological map of regions in north-centred QuACK projection.

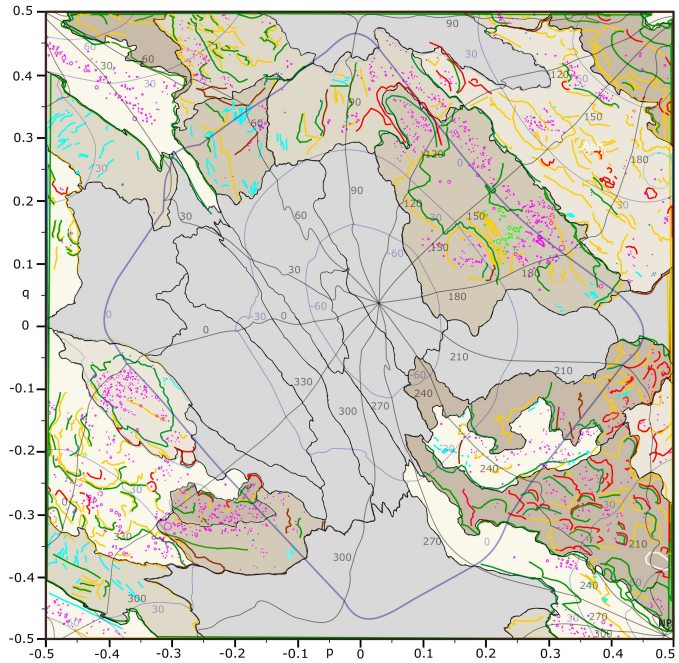

Fig. 13. Combined geological map of regions in south-centred QuACK projection.

and shape of the comet is at the Anuket-Serqet border. This feature is 350 m high and 2500 m long. The sides of the ridge are mostly deserted, with the exception of a few fractures and some boulders at the base.

4.2. Projected geological maps

In this section, we introduce the geological maps we developed for each region. In the background, the maps present the outline of the region, and each sub-region is coloured in a different shade. The provided scale bars are just approximate, as the maps are neither shape nor area preserving, but the projections were chosen to keep distortions as small as possible; see Sect. 3. The geological features described in Sect. 4.1 are displayed according to the legend presented in Table 1. We describe the relation between the subregion definition and the features mapped, as well as the distinctive characteristics of each region. For this analysis, the regions are grouped into five categories that do not correspond to the terrain types we used for the maps in Sect. 3: large-scale depressions, smooth, niche covered, heavily fractured and ridge-separated regions. Figures 12 and 13 illustrate the combined geological map of all regions that can be fully described in the north- and south-centred QuACK layout, respectively.

4.2.1. Large-scale depressions

The geological maps for the depressions of Hatmehit, Aten, and Nut are presented in Fig. 14. As common characteristic, the three regions are delimited by a rim that is superimposed with other features. The rim is not perfectly aligned with the region definition in the case of Hatmehit because the boundary of the depression is not always clear and it can change according to the mapping criteria. In the case of Hatmehit and Aten, the base of the depression is delimited by a closed scarp. The area between the rim and the scarp corresponds to a descending slope, whose steepness is determined by the distance between them. For Hatmehit, this scarp marks the boundary between subregions.

Hatmehit is divided into three sub-regions. The central subregion corresponds to the depression base and is characterised by a large accumulation of boulders. The remaining subregions form the depression border. The darker subregion is less pronounced and slightly fractured. It presents two consecutive niches, one of which rests on the depression rim. The lighter subregion is similar, but steeper and has many terraces. The boulders accumulate closer to the second niche, which suggests a relation to cliff collapse. In this subregion, we identify a set of bright patches in images taken in August 2014. They are located in the areas of steep cliffs, on top of the boulders.

Although Aten is not divided into subregions, it contains characteristic features in the depression base. The only niche in Aten is followed by a terrace, and together, they form the rim of a smaller depression whose base is bounded by a scarp. Within this smaller depression, we find an accumulation of boulders. They are localised in the lower longitudes and latitudes of the region, while the upper latitudes are devoid of boulders.

In Nut, the base of the region is not clearly defined by a single closed scarp. In this case, the rim is covered with terraces and niches that are followed by more gradual slopes that reach the depression base. Nut is also covered by boulders. They are concentrated in the right part of the region.

4.2.2. Smooth regions

In the northern hemisphere, we find the smooth regions of Hapi, Imhotep, and Anubis. We group the geological maps of these three regions in Fig. 15. While Hapi is completely smooth, Anubis and Imhotep present a mix of terrains. Anubis is smooth in the right half of the region and away from the boundary with Seth (upper boundary). Imhotep is smooth primarily in the lighter-coloured subregion, but also inside the niche at the boundary with Khepry. Keeping this in mind, we observe that the smooth

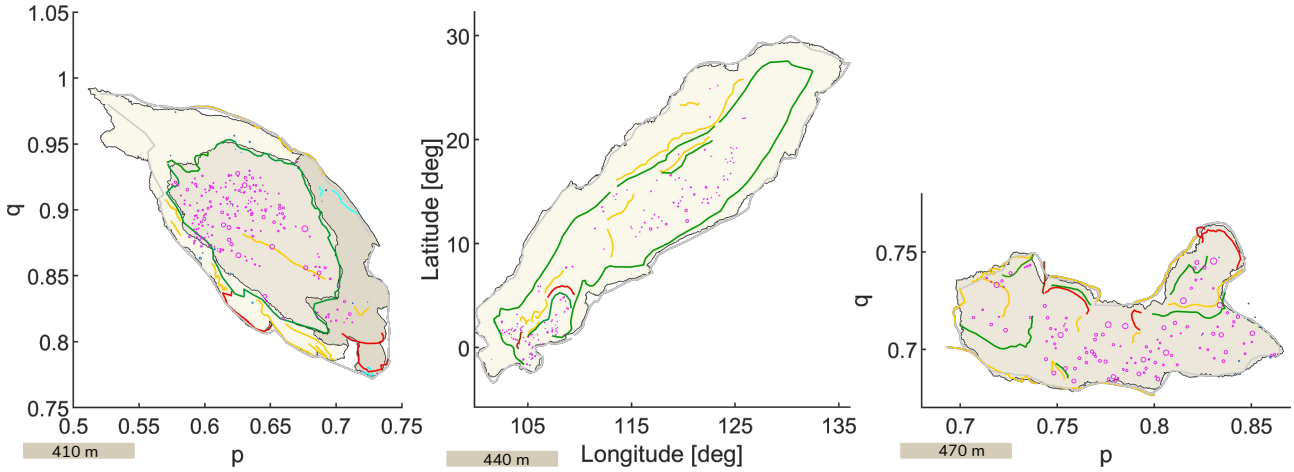

Fig. 14. Geological maps of depressed regions: Hatmehit (*left*), Nut (*right*) in the north-centred QuACK layout, and Aten (*centre*) in the equidistant cylindrical layout with generalised coordinates.

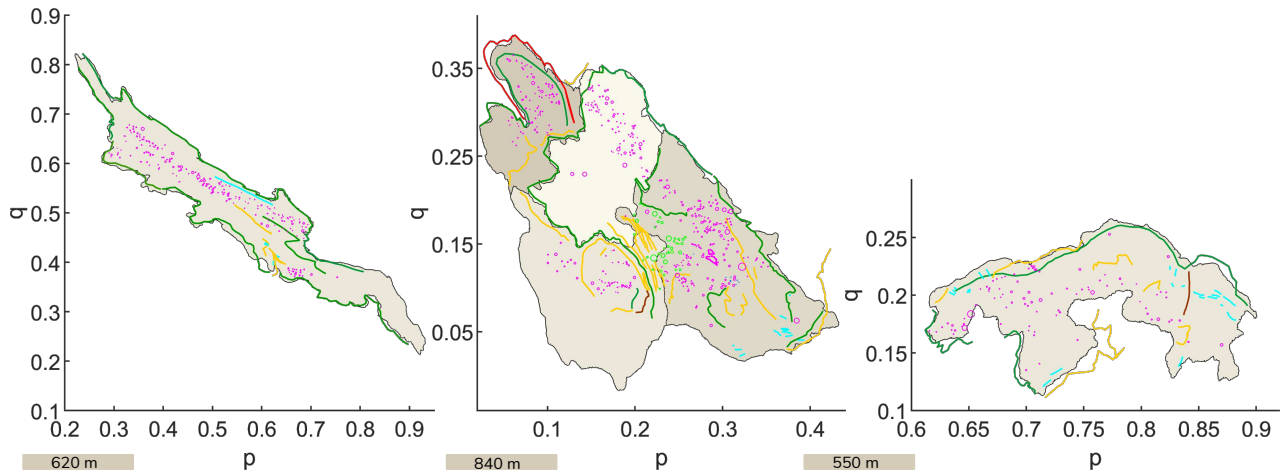

Fig. 15. Geological maps of smooth regions: Hapi (*left*), Anubis (*right*) in north-centred QuACK layout, and Imhotep (*centre*) in the south-centred QuACK layout.

terrains are mostly devoid of features, especially fractures. The only feature that is found consistently and abundantly in the smooth terrains are boulders.

The region of Hapi is completely bounded by a scarp, since it represents the neck of the comet and is completely surrounded by cliffs. The region is covered by boulders, which are aligned in a linear longitudinal pattern. Only some scarps covered by small fractures are found in the region in addition to the long fracture discussed in Sect. 4.1.3.

The Imhotep region is divided into four subregions. Its boundaries are clearly defined by geological features. First, the region lies topographically lower than its neighbours. As a result, the boundaries with Khepry, Ash, and Apis are marked by scarps. The four subregions are very different in terms of terrain and types of features. Starting with the smooth, light-coloured region, it is mostly covered by boulders and is separated from the other regions by scarps. To its left, the region in contact with Khepry also contains smooth patches covered by boulders. The two remaining subregions in the bottom half of Imhotep are marked by a change in morphology. In the right subregion, we find a more consolidated terrain that is covered by boulders and circular mounds and is layered through terraces. The boundary with the left subregion is marked by the transition from the circular mounds to a sequence of smooth terraces.

In Anubis we find a similar behaviour. The boundary with Seth is determined by a scarp, but the boundary with Atum is more complicated and is discussed in Sect. 5. The smooth terrain shows no features except for boulders, and these are mainly found at the scarp boundary with Seth. There is an exception in this case for the ridge found in the smooth part of Anubis, which is particularly wide.

4.2.3. Niche-covered regions

Although niches are present extensively around the northern hemisphere of the comet, in this section, we group the regions with a larger concentration of these features to discuss their similarities and differences. The geological maps for the regions of Anuket, Atum, Ma'at, Ash, and Seth are presented in Fig. 16. We observe that these regions contain several types of niches according to the categories defined in Sect. 4.1.2. This is expected, since the regions themselves cover all longitudes of the comet and have different types of terrains. Anuket and Atum have strongly consolidated terrains. In these regions, the niches are less evident. In Anuket, they are merely small terraces with a hint of curvature that resemble a young niche. For Atum, they are more clearly distinguishable. Ma'at and Ash have dust-covered terrains and both are large regions divided into many subregions.

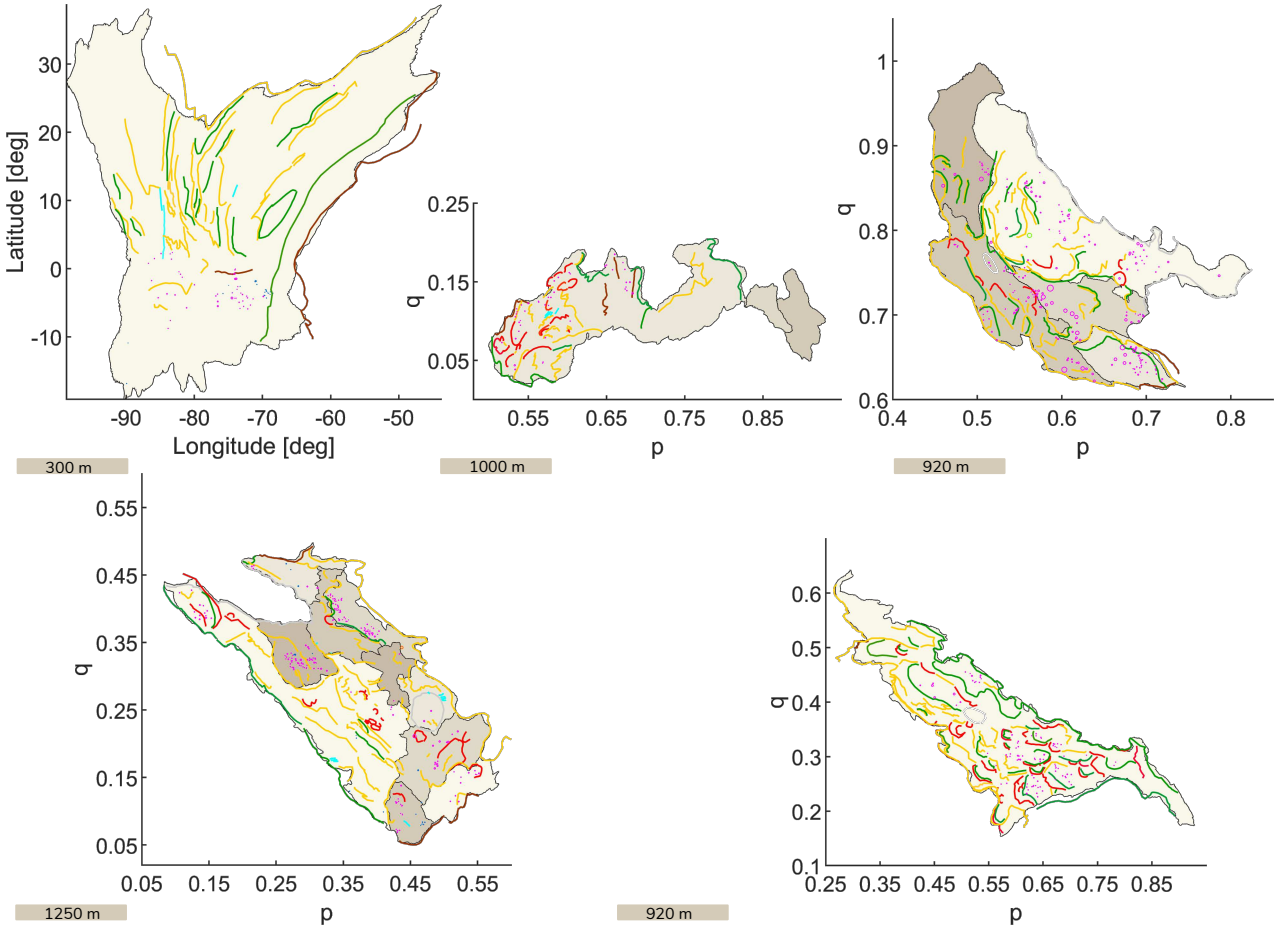

Fig. 16. Geological maps of regions with niche-like features: Anuket (*top left*) in the equidistant cylindrical layout with generalised coordinates and Atum (*top centre*), Ma'at (*top right*), ash (*bottom left*), Seth (*bottom right*) in north-centred QuACK layout.

These regions present niches with similar appearance: scattered, facing multiple directions and without boulders inside. Some of these niches have an almost closed circular shape. Finally, the Seth region has brittle terrain and presents large, deep circular niches facing the same direction.

Anuket is defined as a region without subdivisions. It is bounded by a ridge with Serqet on the right and by a slope change with Hapi on the left. In the interior, we can distinguish two types of surface morphology. In the upper half, corresponding to the northern hemisphere, the surface is covered by a sequence of terraces and scarps and shows two fractures. In the lower half, corresponding to the southern hemisphere, the surface is devoid of linear features and is covered with boulders and a cluster of bright patches. This pattern variation could give rise to the definition of two subregions for Anuket.

Atum is divided into three subregions, although all the features of interest are found in the larger one. The region is bounded with Apis by a scarp to its left and with Ash by a ridge. The boundary with Anubis is more complex and is discussed in more detail in Sect. 5. The terraces and niches are grouped in a portion of the region corresponding to the northern hemisphere and vanish towards the southern hemisphere. In this case, the change of pattern comes with a change of plane along the central scarp. This inclination change is close to 90° and could mark the definition of a fourth subregion.

Ma'at and Ash have very similar characteristics in terms of morphology. Both regions are located at a latitude range between 0° and 60° and cover a large area of the comet. They are higher than the surrounding regions, and therefore the boundaries are defined by terraces and scarps, or by depression rims in the case of the contact with the three large-scale depressions. In Ma'at, the boundaries between subregions are mostly defined by terraces and scarps. In Ash, some subregions are defined by a terrain change, from more consolidated to dust-covered. In Ash, we define a small-scale depression within the region that is outlined in grey. It corresponds to a circular basin with a 400-m diameter. In Ma'at, we observe an elongated pit that is a cylindrical hole on the surface with two boulders at the base.

The region of Seth is bounded by a terrace/scarp with Ash and by scarps with Hapi at the neck and with Anubis and Babi. It is not divided into subregions because its morphology is homogeneous. The region is characterised by a combination of large terraces and niches that are aligned towards the cliff of Hathor. At the centre of the region lies a pit that is 400 m in diameter. Despite the large size of the region, we failed to find any evidence of fractures or bright patches.

4.2.4. Highly fractured regions

Although most of the regions present some type of fracture, here we address the heavily fractured regions of Aker, Apis, and Hathor, see Fig. 17. The first similarity that we find in these regions is that they have strongly consolidated terrain. These regions are not neighbours, and we do not find any apparent

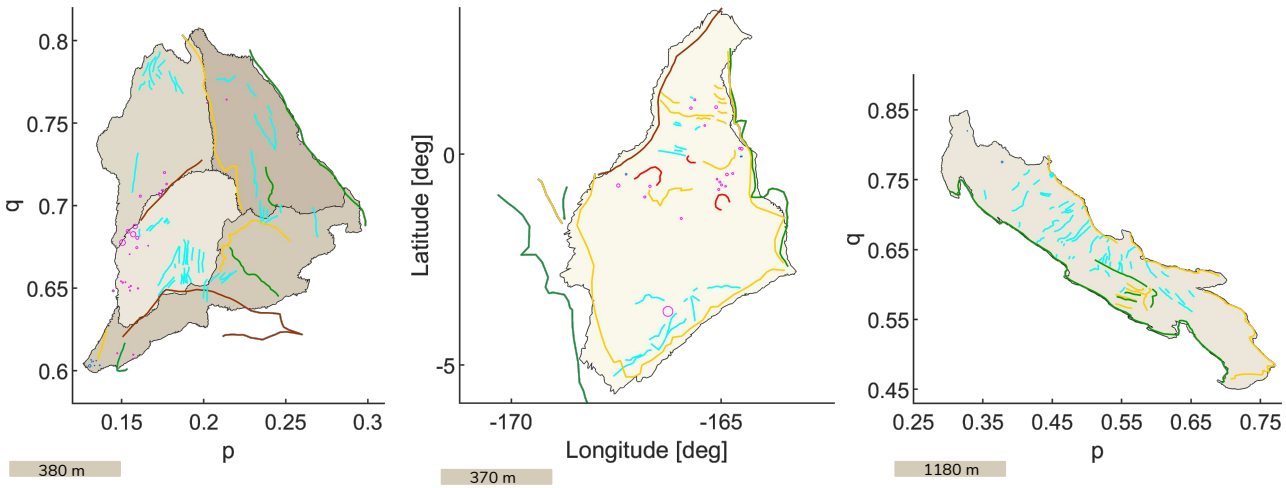

Fig. 17. Geological maps of heavily fractured regions: Aker (*left*), Hathor (*right*) in the north-centred QuACK layout and Apis (*centre*) in the equidistant cylindrical layout with generalised coordinates.

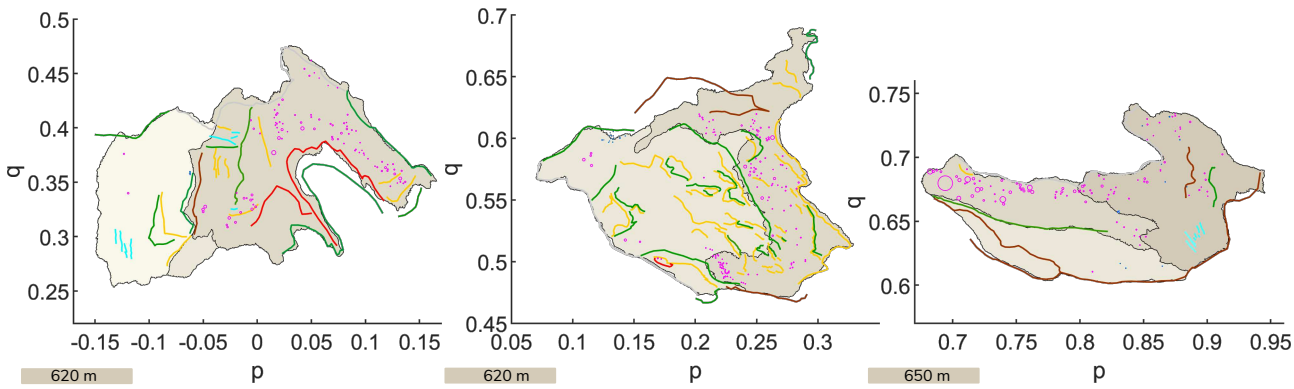

Fig. 18. Geological maps of Khepry (*left*) in the south-centred QuACK layout and Babi (*centre*), and Serqet (*right*) in the north-centred QuACK layout.

relation of the origin of the fractures. While in Hathor and Aker the fractures are aligned roughly in one direction, in Apis we find different patterns.

The Apis region is higher than its surroundings, and therefore its boundary with other regions is delimited by terraces or ridges. The region has a fractured appearance that is reminiscent of elephant skin, although many of these cracks are not wide or clear enough to be mapped. In addition to these linear features, the region is almost bare in the central region. Terraces and boulders are grouped in the upper part of the region, near the boundary with Ash. The fractures are mainly grouped towards the bottom of the region.

Aker consists of four subregions that are clearly defined by geological boundaries. The upper left subregion is a terrace, whose margin creates the boundary with the upper right region. It contains a cluster of fractures near the boundary with Anhur at the top. The upper right region is a cliff that is populated with fractures. The bottom of the cliff marks the boundary with Hapi. The lighter region is bounded by a terrace at the right and by two ridges at the top and bottom. It contains a cluster of fractures at the hillside of the bottom ridge and a cluster of boulders aligned with the top ridge. Finally, the bottom subregion is crossed by the ridge. The boundary with Babi is further discussed in Sect. 5.

Finally, Hathor is the most fractured region, marked with deep long cracks. The region is entirely composed by a cliff, and thus the upper boundary is the margin of the terraces in Ma'at and the lower boundary is the corresponding scarp reaching Hapi. The region is not fully covered by fractures. Near the boundary with Anuket, the cliff encounters a plane change where no linear features are found. Similarly to other regions, this change in morphology could be represented by a different sub-region, bounded by the plane change.

4.2.5. Ridge-separated regions

Finally, we discuss the regions of Khepry, Babi, and Serqet. See Fig. 18 for the geological maps.

Khepry is higher than the surrounding regions, and thus it is separated through scarps from Babi, Ash, and Imhotep, and by a rim from Aten. It is divided into three subregions that are clearly separated through morphological boundaries. To the left, the subregion presents only a few geological features, a small cliff and four fractures. This is different from the right subregion, which is covered by boulders and multiple linear features. The two subregions are separated by a ridge. The small subregion in the lower part is inclined by 90° with respect to the other two, and is bounded by a terrace margin. No features are mapped in it.

The terrain that forms Babi transitions from dust-covered in the lighter left part close to the boundary with Ash to brittle material. This divides the region into two subregions that are physically separated by a scarp. In the lighter subregion we find

several characteristics. In the top left and bottom left corners we find two scarps that delimit the base of two elevated plains. The right half of the subregion contains a sequence of terraces and scarps that form part of a cliff. The left half of the subregion is smooth and covered by dust. The darker subregion is covered by boulders and transitions to a weakly consolidated terrain similar to Seth.

Finally, Serqet is located in the small lobe and is divided into three subregions. The region is bounded by a ridge with Anuket at the bottom and by a rim with Nut at the top. The lower left subregion covers the hillside of the ridge and does not contain any features, except for a boulder and a few bright patches. It is separated from the upper subregion by the scarp of the ridge. The upper left subregion contains an accumulation of boulders that tend to increase in size to the right. The terrain is covered by dust and transitions to more consolidated terrain towards the right subregion.

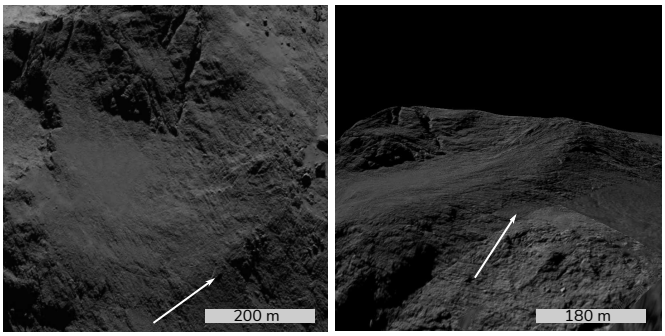

Fig. 19. Example of two-dimensional versus three-dimensional image visualisation. *Left*: close view of a ridge in the Aker region on an OSIRIS NAC image. *Right*: oriented view of the ridge projected onto the comet surface with the SBMT. White arrows mark the ridge location.

5. Discussion and conclusions

The purpose of this work was to conduct an integrated mapping of the northern hemisphere of comet 67P and to display the results in an unambiguous projection. In the new geological maps we identified the boundaries that define regions and subregions. Moreover, we identified the characteristics of each type of geological feature. In this section, we first discuss the advantages of the approach we used for the mapping, then we propose some regional updates, and finally, we introduce suggestions for future work.

5.1. Advantages of mapping in three dimensions

When unprojected OSIRIS products are mapped, the two-dimensional images cannot be superimposed. Different images are taken at different altitudes and locations and cannot be directly combined. In the two-dimensional approach, a single image is therefore used to map a complete region. This requires selecting lower-resolution images that are taken from higher altitudes. The SBMT projects the images onto the comet surface. They can then can be overlapped. In the three-dimensional approach, several smaller and higher resolution images taken at a lower altitude can therefore be selected to cover a single region. This expands the range of features that can be identified. For example, a previous geological mapping uses two images to map the features located in the regions of Nut, Hatmehit, Ma'at, Serqet, and Hathor of the small lobe (see Giacomini et al. 2016, Figs. 11 and 12). As a result, many features have not been identified, especially in the regions of Nut and Serqet, which are located at the limb. The features located at the horizon of the image are distorted or even appear to be superimposed. This occurs with the mapping of boulders in the Hapi region by Pajola et al. (2015). Dozens of features are located close to the limb and collapse into a single front of overlapping boulders (see Pajola et al. 2015, Fig. 8F). With the SBMT approach, we ensure that the mapping is performed with multiple high-resolution images. Moreover, the features on the comet are three-dimensional, and mapping on two-dimensional views can cause interpretation errors. For example, it can be difficult to distinguish between depressions and outcrops because the position of the shadows in an image can be misleading. The SBMT allows navigating across the comet and observing the same feature in several images and from different angles, which reduces the ambiguity. Figure 19 presents an example of this effect. On the left we find a close view covering the Aker region. In this image, we find a linear feature highlighted with a white arrow, whose appearance cannot be fully constrained. It could be a terrace, but also a ridge or a canyon. On the right we find an oriented view of the same image projected onto the SHAP4S shape model of the comet. In this case, we clearly conclude that the feature is a ridge. Similarly to this case, the SBMT has proven to be extremely useful in determining the type of features in many occasions.

5.2. Minor regional updates

With the analysis from a global perspective of the geological features we mapped, we confirmed previous results and learned more about the comet. First, we verified that the regional unit boundaries defined by Thomas et al. (2015) are aligned in most cases with linear features that were mapped independently. In some cases, the boundary only partially corresponds to a feature or is determined by gradual changes in terrain that cannot be defined by a feature. In two cases, the region definition is not aligned with the morphology and does not follow the criteria governing other boundaries. For these cases, we propose minor modifications of the region boundaries.

First, we revisit the Anubis–Atum boundary. The original boundary is formed by a scarp and a transition from smooth to consolidated terrain. However, the central segment of the boundary is not aligned with any particular feature or terrain variation. Approximately 100 m to the right of this boundary segment, we find a terrace margin that marks a clear division between the plain where Anubis is found and the lower portion of Atum. The terrace is followed by a 90° change in inclination. Therefore we suggest that this feature is better suited for a definition of the boundary between Anubis and Atum. Figure 20 illustrates this. At the top, in a lighter background we find the Anubis region with its features. At the bottom, in a darker background, lies the Atum region. The hatched region originally corresponded to Atum, and we propose to include this area in Anubis, shifting the boundary to match the terrace.

Second, we propose a modification in the Aker-Babi frontier. Originally, the boundary is crossed by a large ridge, the upper half of which belongs to Aker and the lower half to Babi. The lowest section of the boundary is marked by a slope change. However, because we do not find any morphological differences between the upper and lower half of the ridge that justify their inclusion in different regions, we suggest to modify the boundary so that it is aligned with the ridge. Figure 21 presents Aker at the top in a lighter background and Babi at the bottom in a darker

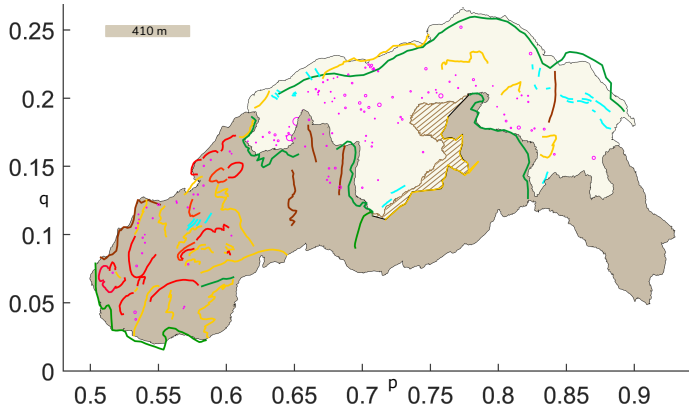

Fig. 20. Proposed change in boundary between regions Anubis (*top light*) and Atum (*bottom dark*). The hashed area originally corresponded to Atum and is proposed to form part of Anubis. The new boundary follows the terrace.

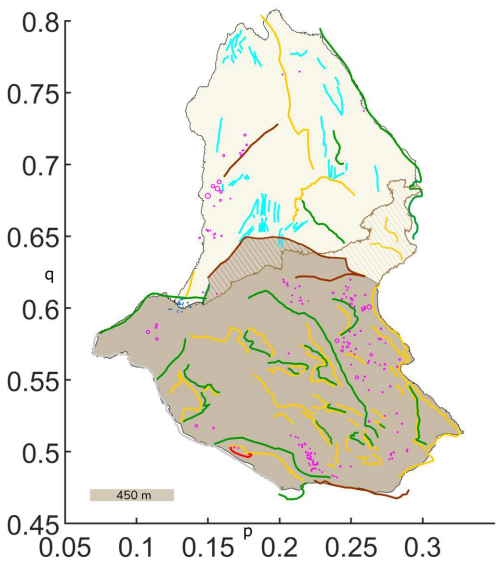

Fig. 21. Proposed change in boundary between regions Aker (*top light*) and Babi (*bottom dark*). The hashed area with light background originally corresponded to Babi and is proposed to form part of Aker. The hashed area with dark background originally corresponded to Aker and is proposed to form part of Babi. The new boundary follows the ridge.

background. It is clear that the ridge transverses the original boundary. We propose that the hatched area with darker background (which originally formed Aker) is assigned to Babi, and the hatched area with lighter background is assigned to Aker. In this way, the ridge of the mountain range would mark the separation between regions. The subregions can be extended to include the new areas following the same criteria as before.

5.3. Recommendations for future surface investigations

The mapping we produced is incomplete because it does not include some of the regions in the southern hemisphere that were shadowed during the observation period available in the SBMT. If the map of these regions were included, it would provide a complete understanding of the comet morphology.

A dichotomy between the northern and southern hemisphere has been detected in terms of morphology (El-Maarry et al. 2016) and volatile sublimation (Hoang et al. 2017). In comparison to the northern hemisphere, the southern regions appear to be smoother. One of the most interesting results of the mapping is the clear confirmation of the north-south dichotomy in the Anuket and Atum regions. In these locations, the surface features change abruptly within few degrees of latitude. In both cases the surface is heavily terraced in the northern hemisphere and flattens directly after the equatorial line. In Atum, the northern section is covered with niches in addition to terraces, which also dim out towards the south. The dichotomy between the hemispheres was observed as a general trend even in the first observations, but these maps provide specific locations in which the effect occurs sharply. The association of these maps with proper modelling of cometary processes will certainly help to understand the surface morphology of 67P better.

Another relevant finding is the location of 150 new bright patches during the first three months of observations of the Rosetta mission. These complement the 56 other bright patches found by previous researchers (Deshapriya et al. 2018) in the two years of Rosetta observations. The bright patches can be correlated with many parameters, such as the received solar flux, the orbital position, and the change in morphology. Following the procedure by Barucci et al. (2016) to obtain results without spurious data, our results and maps provide unambiguous locations of new potential bright patches that could be easily identified in the observations of other instruments on board the Rosetta mission, including the VIRTIS spectrometer.

Finally, the mapping has produced a large database of features with their location, length, or diameter. With these data, a statistical analysis of the features could be performed depending on their coordinates and radius to determine how they are distributed on the comet. This information can be valuable for understanding the relation of the features and evolutionary processes that occur in the comet, and its morphology as a whole (Penasa et al. 2017). A further step can be to relate these statistics with results from mapping of other Jupiter-family comets. In this way, further understanding would be achieved to better understand whether cometary nuclei have a common past and evolution, or if there are dependences on the initial comet shape or other factors.

6. Summary

The approach followed to integrate the features of comet 67P onto a single framework has produced the following outcomes.

First, a set of global projections based on a QuACK map of the entire surface of comet 67P that is suitable for different applications. This was made possible with the use of innovative techniques that allow the treatment of complex and irregular shapes in a two-dimensional representation. Second, a set of individual geological maps for the northern hemisphere, which are displayed on OSIRIS images and in QuACK map projections. Third, a set of geological landmarks for the northern hemisphere that significantly expand on the complexity of the morphology of comet 67P. All these products are available at the ESA Guest Storage Facility (European Space Agency, 2021, ESA-AURORA_67P-GEOMAP_OSIRIS_V1.0,[4]).

The analysis of these maps has shown that regions of the comet's surface share common traits that allow us to expand our knowledge about the formation processes of the comet. Using these customised visualisation and projections, we propose minor updates to two boundaries between Anubis and Atum, and Aker with Babi.

[4] https://doi.org/10.5270/esa-kokoti7

The methods and techniques presented have the potential to largely benefit further investigations of comet 67P and other highly irregular bodies like, such as Arrokoth (MU_{69}, Stern et al. 2019).

Acknowledgements. The authors thank the European Space Research and Technology Centre and the European Space Astronomy Centre faculty councils for supporting this research. M. Leon-Dasi was supported by an internship from the European Space Agency (ESA) at the European Space Astronomy Centre, Madrid, in the period March to December 2020.

References

A'Hearn, M. F., Belton, M. J. S., Delamere, W. A., et al. 2005, Science, 310, 258
A'Hearn, M. F., Belton, M. J. S., Delamere, W. A., et al. 2011, Science, 332, 1396
Auger, A.-T., Groussin, O., Jorda, L., et al. 2015, A&A, 583, A35
Barucci, M. A., Filacchione, G., Fornasier, S., et al. 2016, A&A, 595, A102
Besse, S., Küppers, M., Barnouin, O. S., Thomas, N., & Benkhoff, J. 2014, Planet. Space Sci., 101, 186
Besse, S. B., Guilbert-Lepoutre, A., Vincent, J.-B., Bodewits, D., & Pajola, M. 2015, in European Planetary Science Congress, EPSC2015-114
Besse, S., Vallat, C., Barthelemy, M., et al. 2018, Planet. Space Sci., 150, 131
Birch, S. P. D., Tang, Y., Hayes, A. G., et al. 2017, MNRAS, 469, S50
Brownlee, D. E., Horz, F., Newburn, R. L., et al. 2004, Science, 304, 1764
Deshapriya, J. D. P., Barucci, M. A., Fornasier, S., et al. 2018, A&A, 613, A36
El-Maarry, M. R., Thomas, N., Giacomini, L., et al. 2015, A&A, 583, A26
El-Maarry, M. R., Thomas, N., Gracia-Berná, A., et al. 2016, A&A, 593, A110
El-Maarry, M. R., Groussin, O., Thomas, N., et al. 2017, Science, 355, 1392
Ernst, C. M., Barnouin, O. S., Daly, R. T., & Small Body Mapping Tool Team. 2018, in Lunar and Planetary Science Conference, Lunar Planet. Sci. Conf., 1043
Filacchione, G., Groussin, O., Herny, C., et al. 2019, Space Sci. Rev., 215
Fornasier, S., Hoang, V. H., Hasselmann, P. H., et al. 2019, A&A, 630, A7
Giacomini, L., Massironi, M., El-Maarry, M. R., et al. 2016, MNRAS, 462, S352
Grieger, B. 2019, A&A, 630, A1
Grieger, B. 2020, Optimized global map projections for specific applications: the triptychial projection and the Spilhaus projection, EGU General Assembly 2020, https://doi.org/10.5194/egusphere-egu2020-9885
Groussin, O., Sierks, H., Barbieri, C., et al. 2015, A&A, 583, A36
Hoang, M., Altwegg, K., Balsiger, H., et al. 2017, A&A, 600, A77
Keller, H. U., Arpigny, C., Barbieri, C., et al. 1986, Nature, 321, 320
Keller, H. U., Barbieri, C., Lamy, P., et al. 2007, Space Sci. Rev., 128, 433
Kohonen, T. K. 1982, Biol. Cybernet., 43, 59
Lara, L. M., Lowry, S., Vincent, J.-B., et al. 2015, A&A, 583, A9
Lee, J.-C., Massironi, M., Ip, W.-H., et al. 2017, MNRAS, 462, S573
Massironi, M., Da Deppo, V., Magrin, S., et al. 2015, Nature, 526
Pajola, M., Vincent, Jean-Baptiste, Güttler, Carsten, et al. 2015, A&A, 583, A37
Peirce, C. S. 1879, Am. J. Math., 2, 394
Penasa, L., Massironi, M., Naletto, G., et al. 2017, MNRAS, 469, S741
Preusker, F., Scholten, F., Matz, K.-D., et al. 2015, A&A, 583, A33
Preusker, F., Scholten, F., Matz, K.-D., et al. 2017, A&A, 607, L1
Sagdeev, R. Z., Szabo, F., Avanesov, G. A., et al. 1986, Nature, 321, 262
Schmitt, M. I., Tubiana, C., Güttler, C., et al. 2017, MNRAS, 469, S380
Sierks, H., Barbieri, C., Lamy, P. L., et al. 2015, Science, 347, aaa1044
Soderblom, L. A., Becker, T. L., Bennett, G., et al. 2002, Science, 296, 1087
Stern, S. A., Weaver, H. A., Spencer, J. R., et al. 2019, Science, 364, https://science.sciencemag.org/content/364/6441/eaaw9771.full.pdf
Thomas, N., Sierks, H., Barbieri, C., et al. 2015, Science, 347, https://science.sciencemag.org/content/347/6220/aaa0440.full.pdf
Thomas, N., El Maarry, M. R., Theologou, P., et al. 2018, Planet. Space Sci., 164, 19
Vincent, J.-B., Bodewits, D., Besse, S., et al. 2015, Nature, 523, 63
Vincent, J.-B., A'Hearn, M. F., Lin, Z. Y., et al. 2016, MNRAS, 462, S184
Vincent, J.-B., Birch, S., Hayes, A., et al. 2019, in EPSC Abstracts, 13

Appendix A: Image list

Table A.1. OSIRIS NAC images used in this work and their corresponding ID in the PSA.

Figure	Location	Image ID
Fig. 3	top-left	N20140911T183453085ID4CF41
	top-right	N20140905T063200151ID4BF16
	bottom-left	N20141001T235606564ID4BF22
	bottom-right	N20140919T092005015ID4DF41
Fig. 4	left	N20140914T173203723ID20F24
	right	N20140915T035843369ID20F16
Fig. 5	left	N20140905T063640163ID20F16
	right	N20140910T183429960ID20F23
Fig. 10		N20140914T042801354ID30F22
		N20140914T165607330ID30F22
		N20140914T173203723ID30F24
		N20140915T054212353ID30F22
Fig. 19	left	N20140915T035831347ID4BF22
	right	N20140905T092146752ID30F27
		N20140915T032356359ID30F22
		N20140915T035831347ID30F22
		N20140915T043304393ID30F22
Fig. B.1		N20140905T064555557ID30F22
		N20140905T080610114ID30F23
		N20140905T081055531ID30F22
		N20140905T081209321ID30F41
		N20140912T232115888ID30F24
Fig. B.2		N20140905T023709361ID30F41
		N20140905T024055548ID30F22
		N20140913T192343364ID30F22
		N20140913T204840352ID30F22
		N20140914T202827768ID30F24
		N20140916T094348370ID30F22
Fig. 11		N20140913T130124352ID30F22
		N20140913T134431962ID30F24
		N20140914T151056102ID30F24
Fig. B.3		N20140905T053209353ID30F41
		N20140919T045716392ID30F22
		N20140919T162740801ID30F24
Fig. B.4		N20140905T053209353ID30F41
		N20140905T053555525ID30F22
		N20140905T063216361ID30F28
		N20140905T063555557ID30F22
		N20140905T063709443ID30F41
		N20140905T064209480ID30F41
Fig. B.5		N20140905T023231389ID30F41
		N20140905T024654450ID30F28
Fig. B.6		N20140823T154254636ID30F22
Fig. B.7		N20140829T154253562ID30F22
Fig. B.8		N20140806T024316574ID30F22

Table A.1. continued.

Figure	Location	Image ID
Fig. B.9		N20140914T035114860ID30F24
		N20140914T050608153ID30F24
		N20140912T031020675ID30F23
		N20140913T150928587ID30F24
		N20140913T163348359ID30F22
		N20140914T035114860ID30F24
		N20140807T232034548ID30F22
		N20140807T233734573ID30F22
Fig. B.10		N20140914T174834649ID30F24
		N20140914T184236144ID30F24
		N20140915T063400344ID30F22
Fig. B.11		N20140905T080709325ID30F41
		N20140913T110928393ID30F23
		N20140905T053124788ID30F27
		N20140911T183441014ID30F24
		N20140912T063423569ID30F23
		N20140913T094727926ID30F24
		N20140913T204919937ID30F24
		N20140910T183400345ID30F22
		N20140910T201407346ID30F22
		N20140911T214940552ID30F41
Fig. B.12		N20140807T203734564ID30F22
Fig. B.13		N20140913T171616345ID30F22
		N20140914T054255346ID30F22
		N20140914T184156338ID30F22
		N20140915T065201377ID30F22
		N20140915T072719335ID30F22
Fig. B.14		N20140905T092146752ID30F27
		N20140915T032356359ID30F22
		N20140915T035831347ID30F22
		N20140915T043304393ID30F22
Fig. B.15		N20140905T081124821ID30F27
		N20140905T081155316ID30F28
		N20140905T092216367ID30F28

Appendix B: Identification of features in OSIRIS images

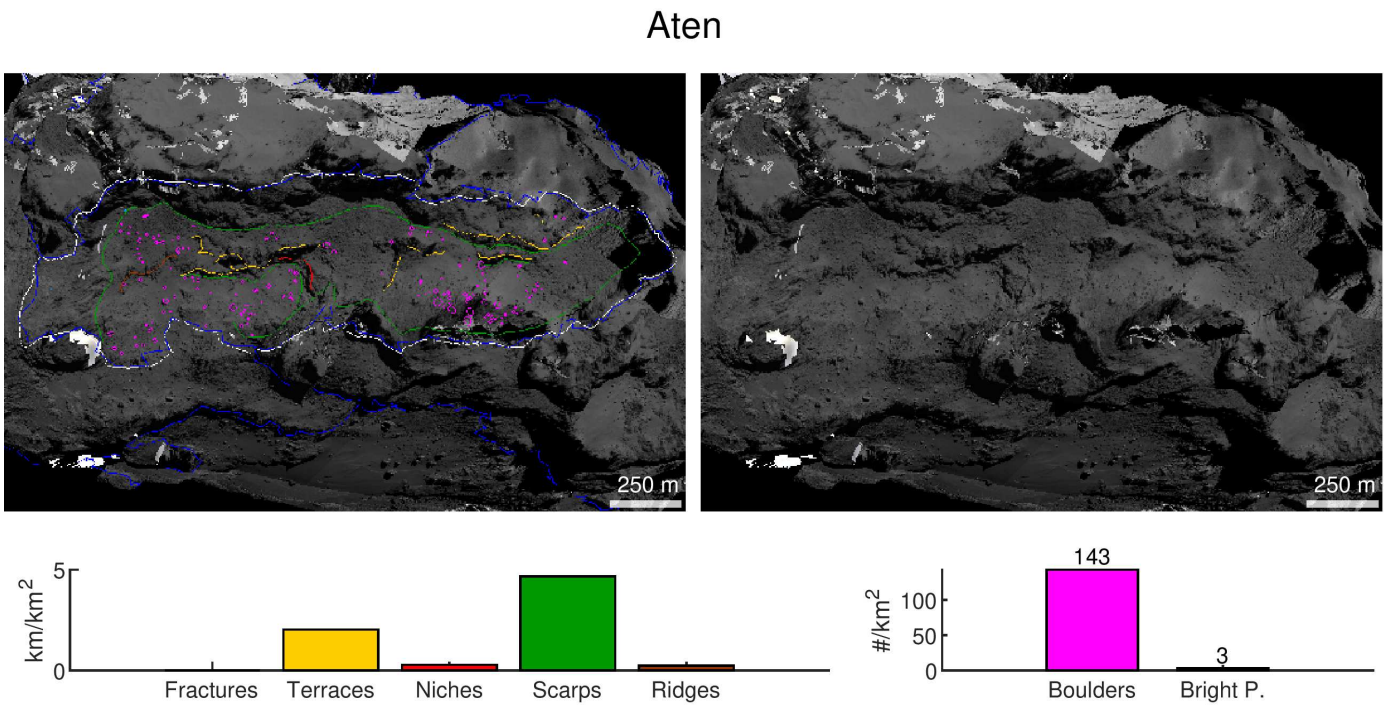

Fig. B.1. Identification of features in the Aten region from images projected onto the SHAP4S shape model and annotated on the SBMT.

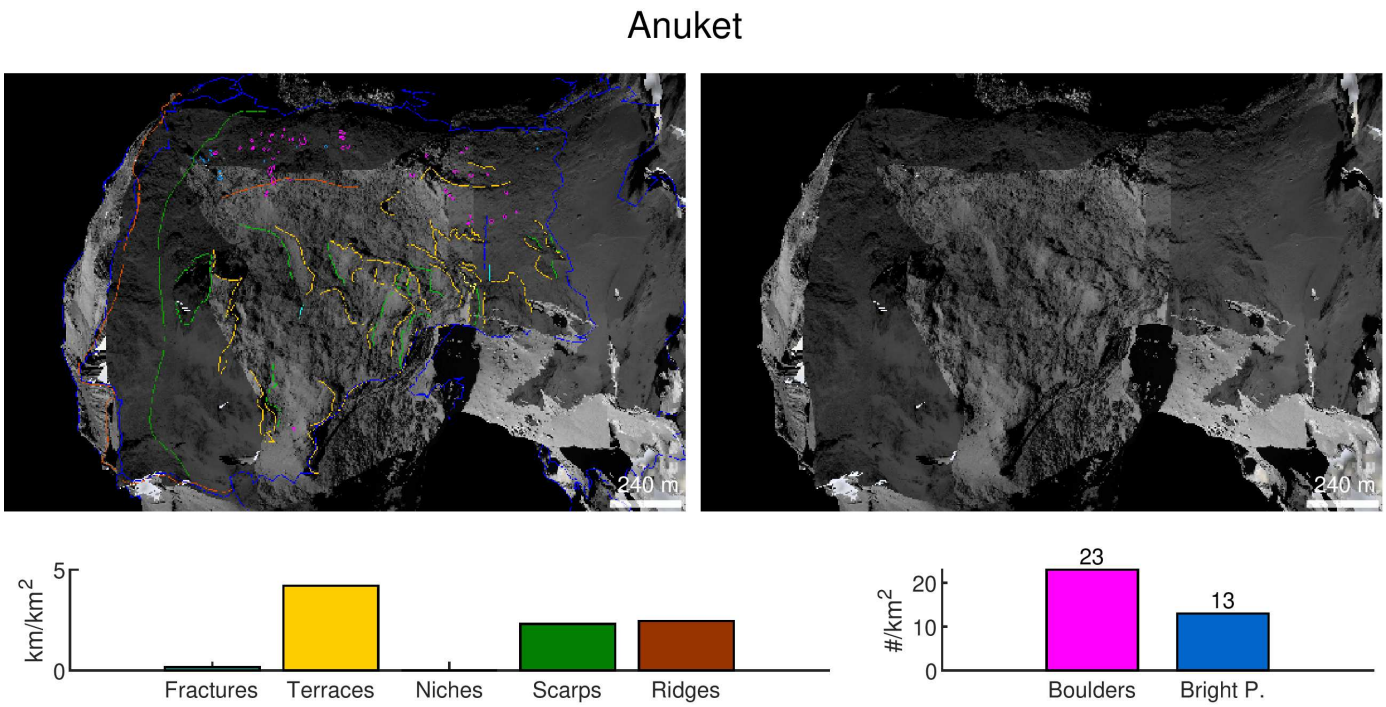

Fig. B.2. Identification of features in the Anuket region from images projected onto the SHAP4S shape model and annotated on the SBMT.

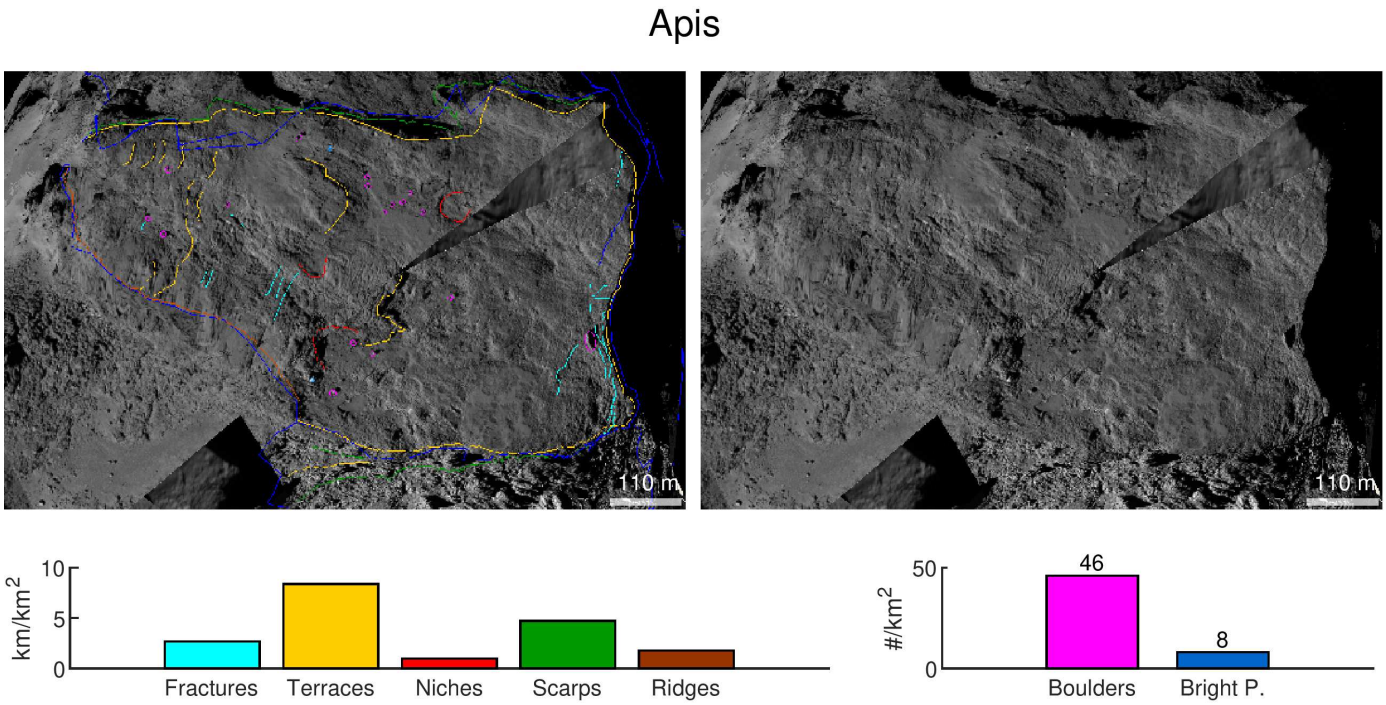

Fig. B.3. Identification of features in the Apis region from images projected onto the SHAP4S shape model and annotated on the SBMT.

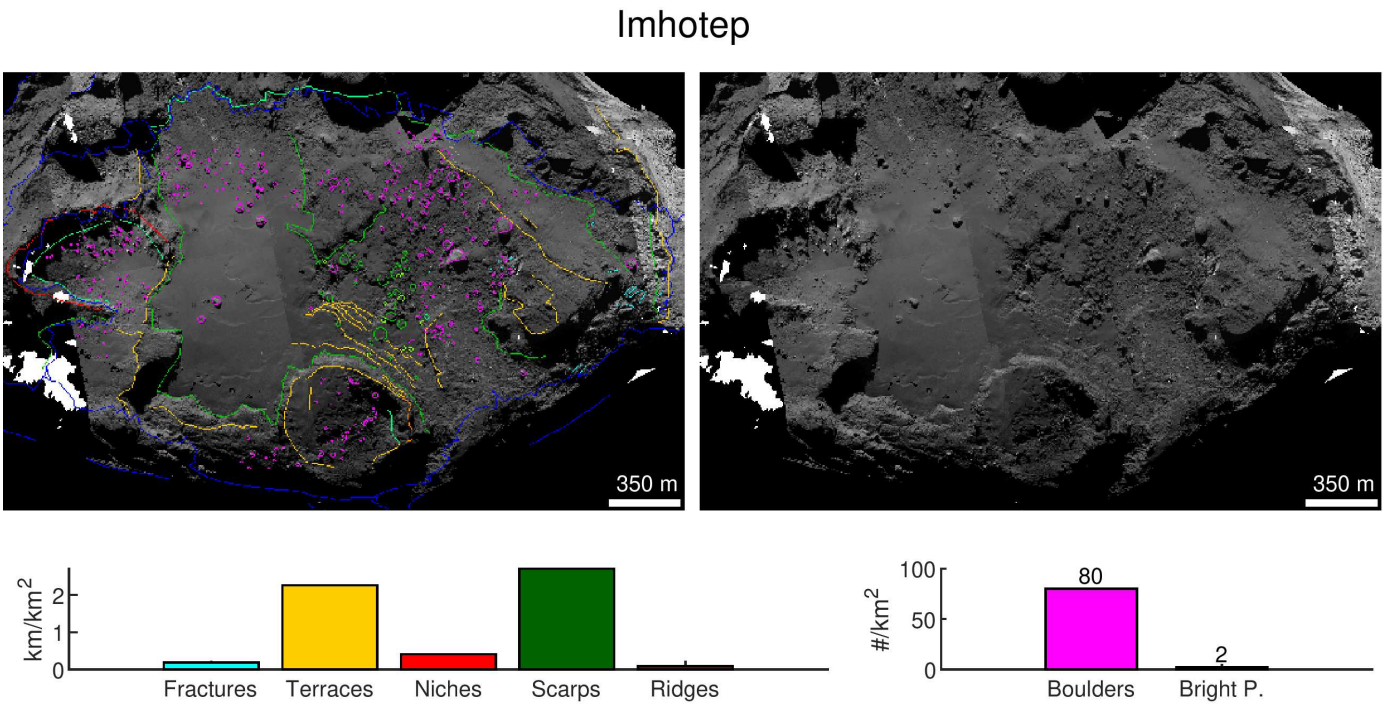

Fig. B.4. Identification of features in the Imhotep region from images projected onto the SHAP4S shape model and annotated on the SBMT.

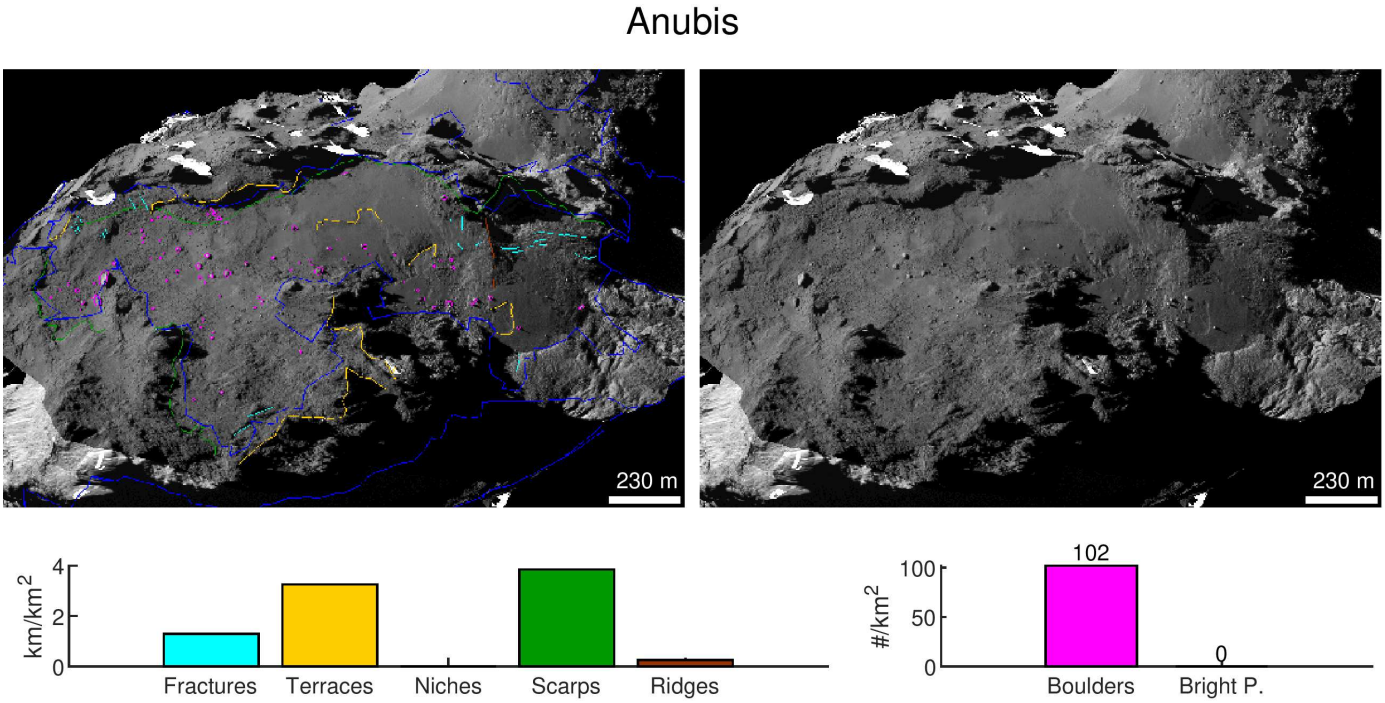

Fig. B.5. Identification of features in the Anubis region from images projected onto the SHAP4S shape model and annotated on the SBMT.

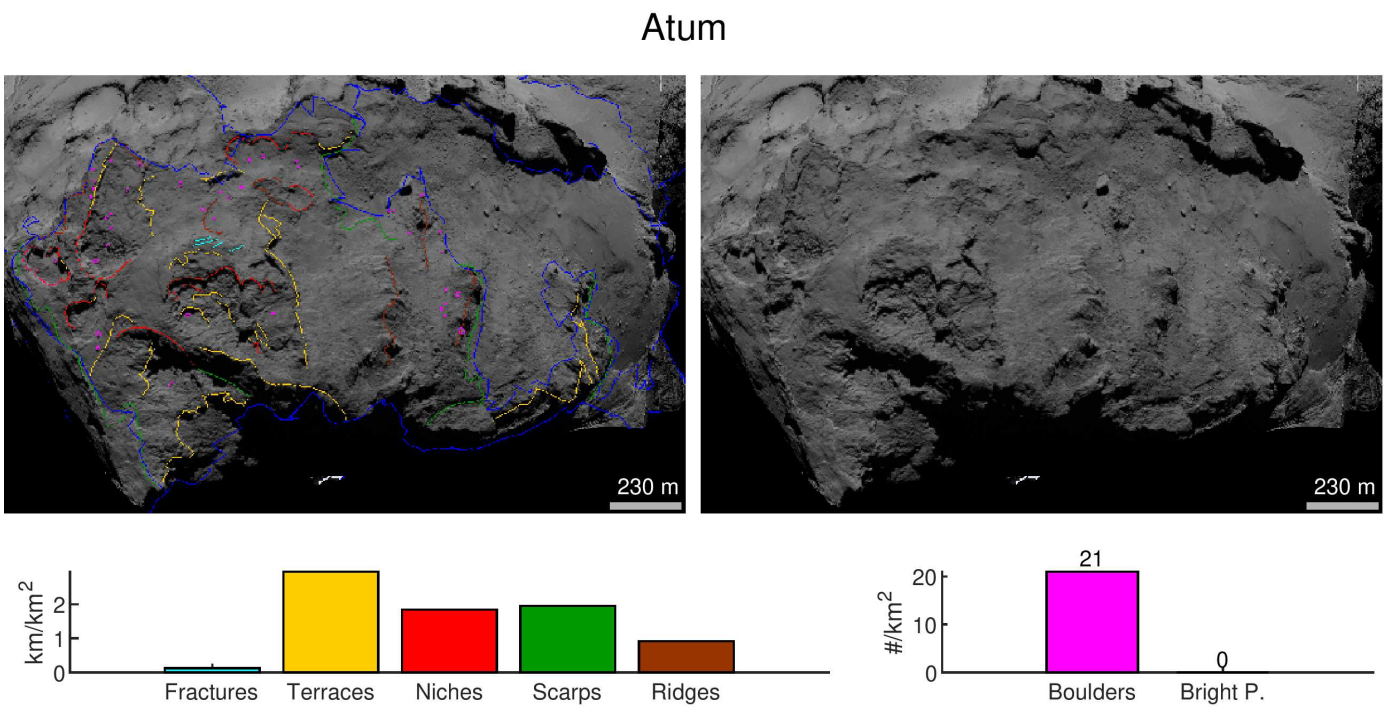

Fig. B.6. Identification of features in the Atum region from images projected onto the SHAP4S shape model and annotated on the SBMT.

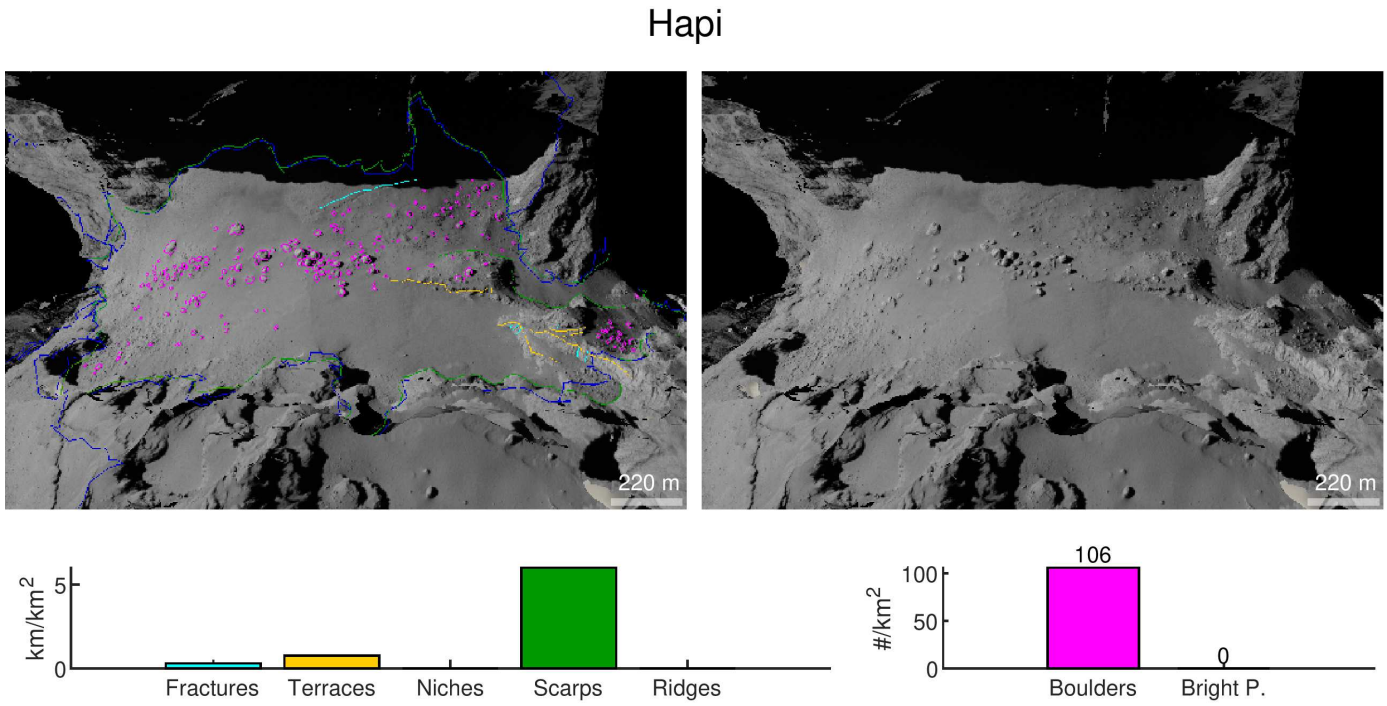

Fig. B.7. Identification of features in the Hapi region from images projected onto the SHAP4S shape model and annotated on the SBMT.

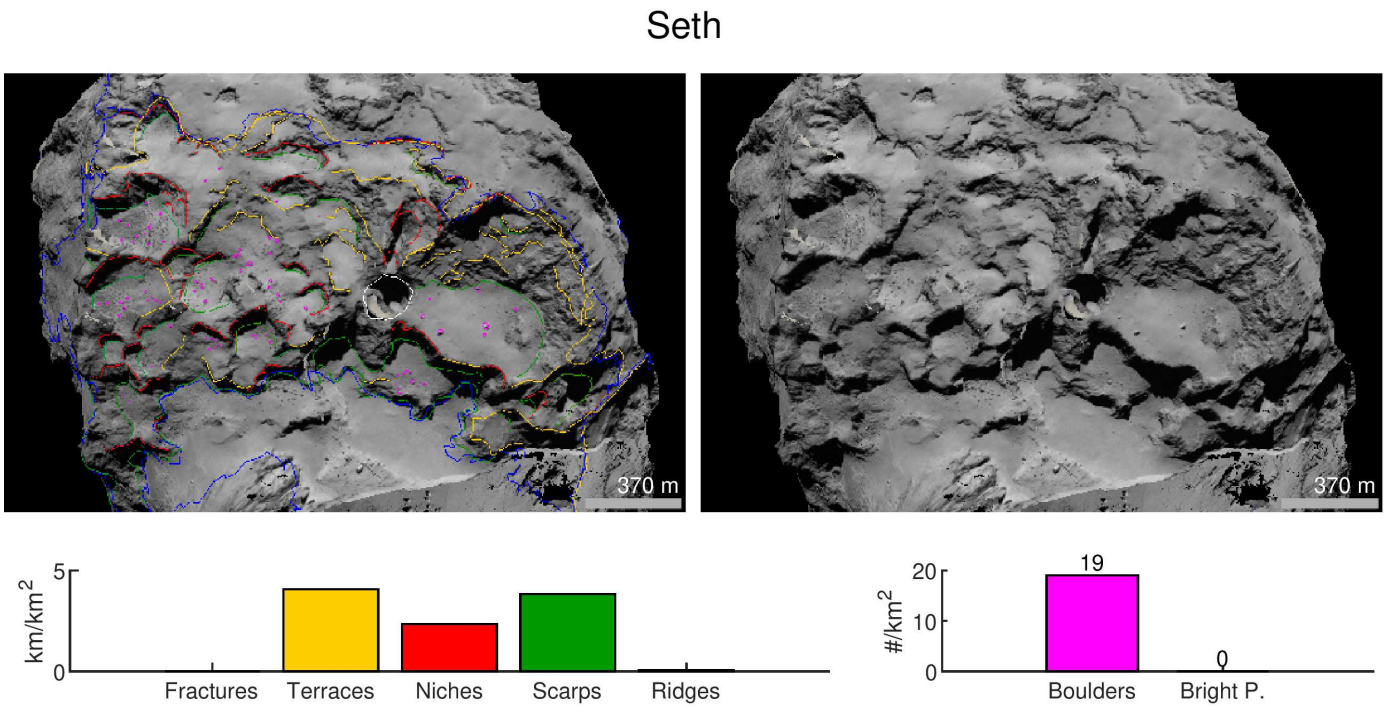

Fig. B.8. Identification of features in the Seth region from images projected onto the SHAP4S shape model and annotated on the SBMT.

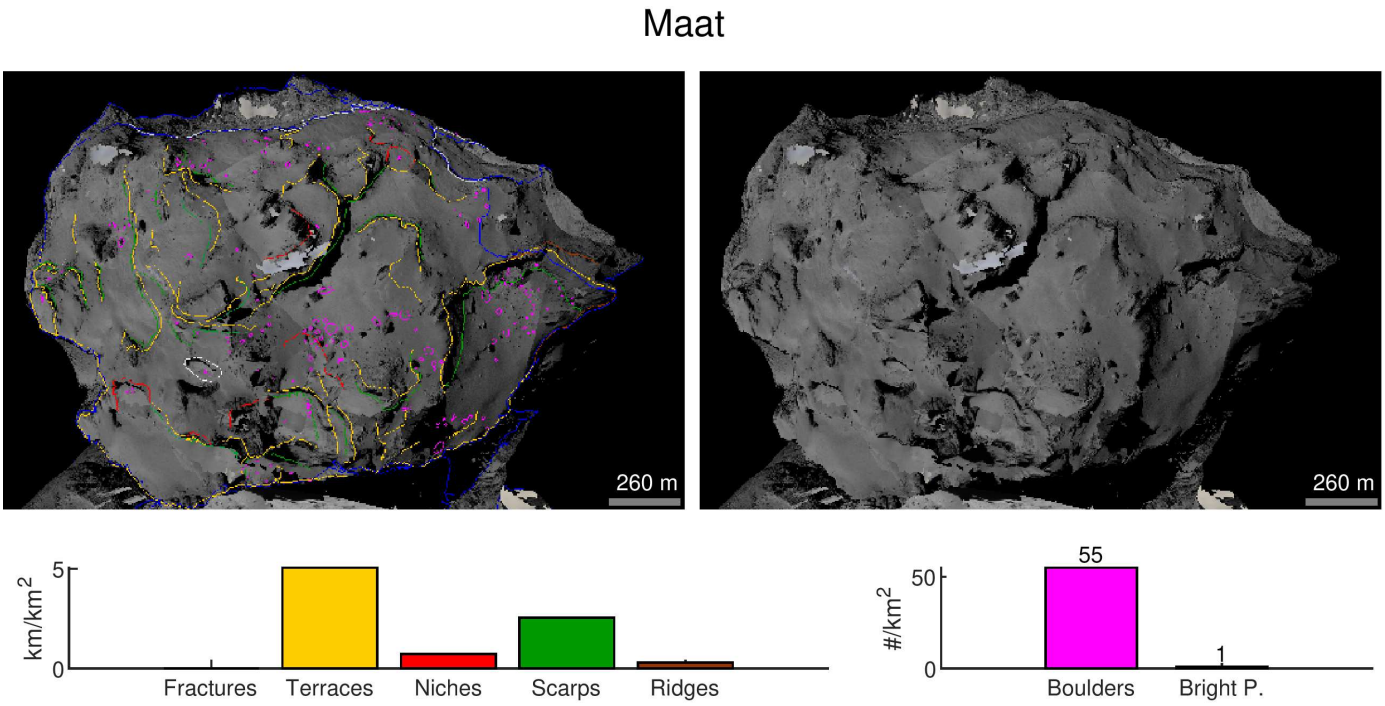

Fig. B.9. Identification of features in the Ma'at region from images projected onto the SHAP4S shape model and annotated on the SBMT.

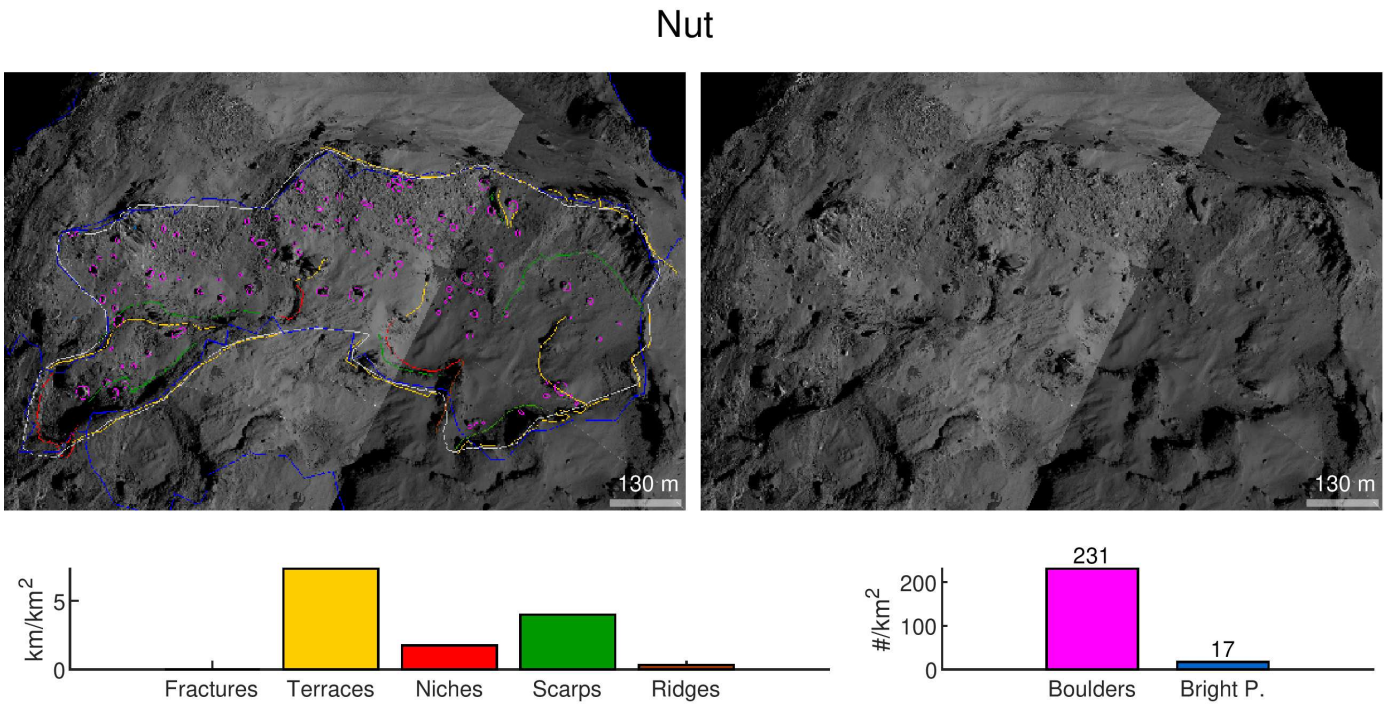

Fig. B.10. Identification of features in the Nut region from images projected onto the SHAP4S shape model and annotated on the SBMT.

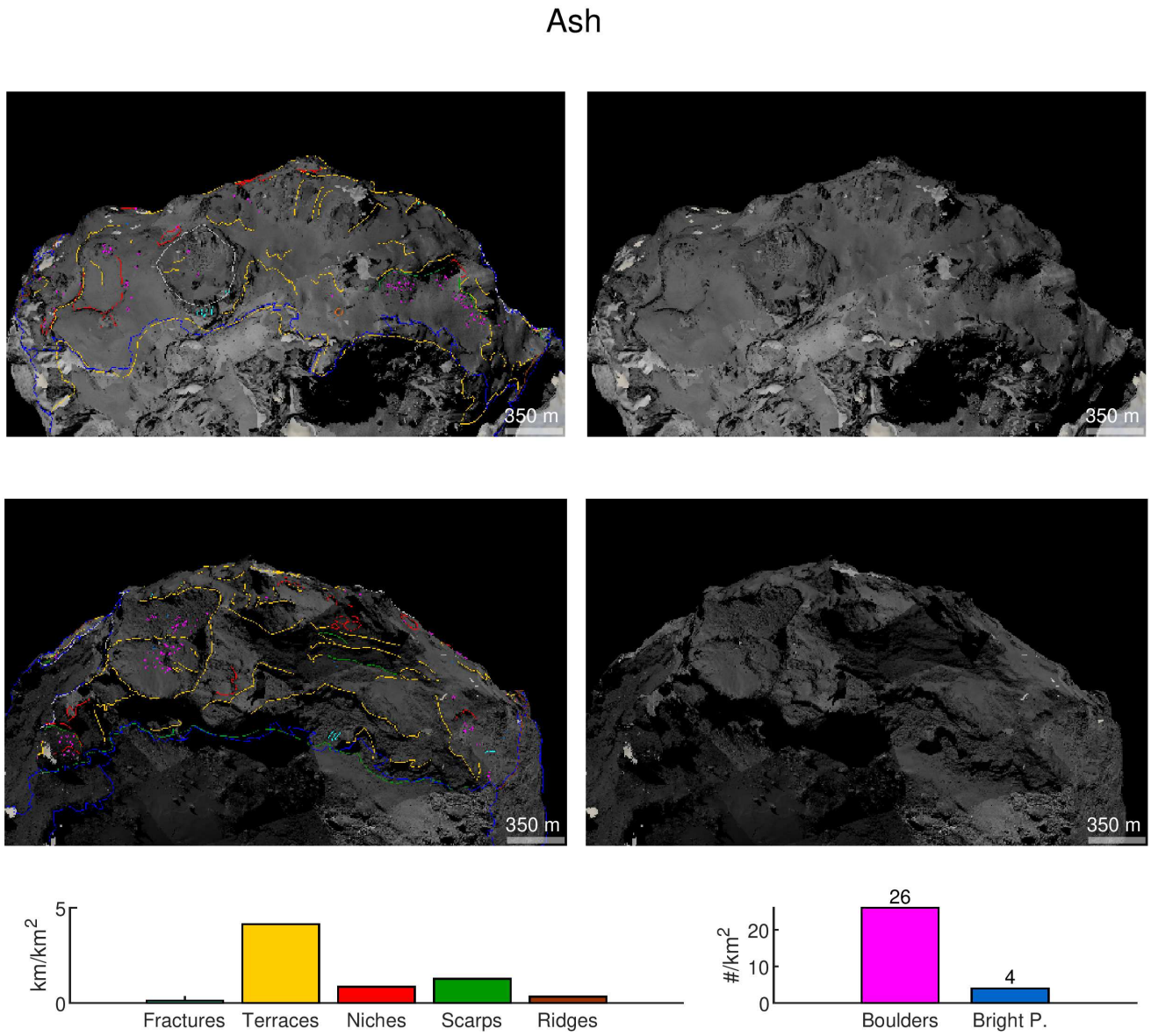

Fig. B.11. Identification of features in the Ash region from images projected onto the SHAP4S shape model and annotated on the SBMT.

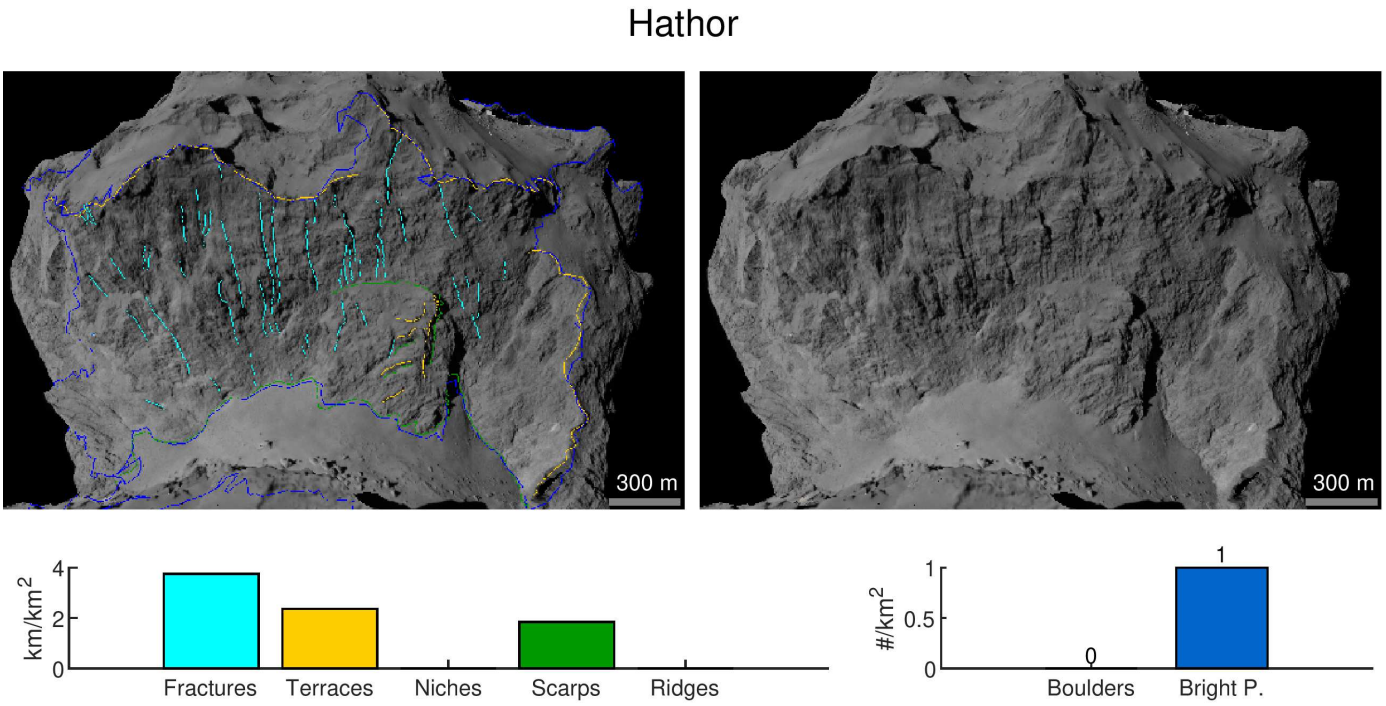

Fig. B.12. Identification of features in the Hathor region from images projected onto the SHAP4S shape model and annotated on the SBMT.

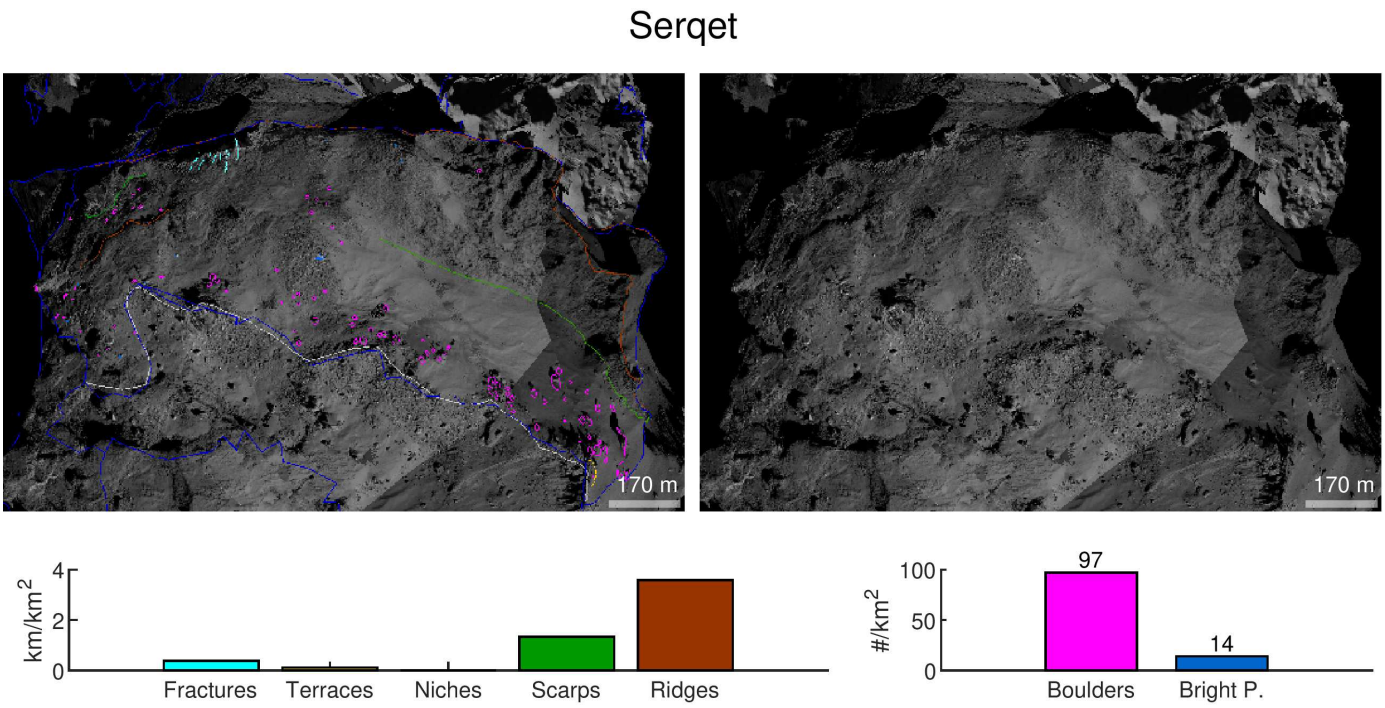

Fig. B.13. Identification of features in the Serqet region from images projected onto the SHAP4S shape model and annotated on the SBMT.

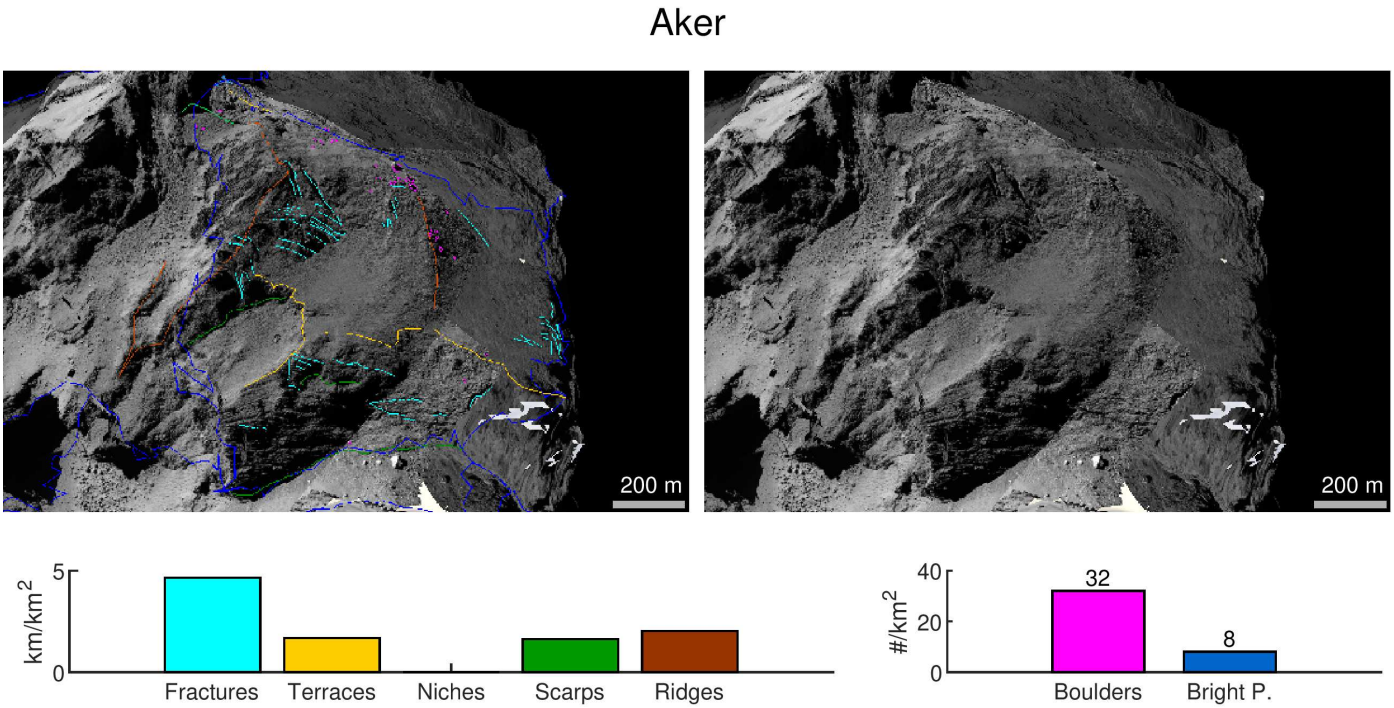

Fig. B.14. Identification of features in the Aker region from images projected onto the SHAP4S shape model and annotated on the SBMT.

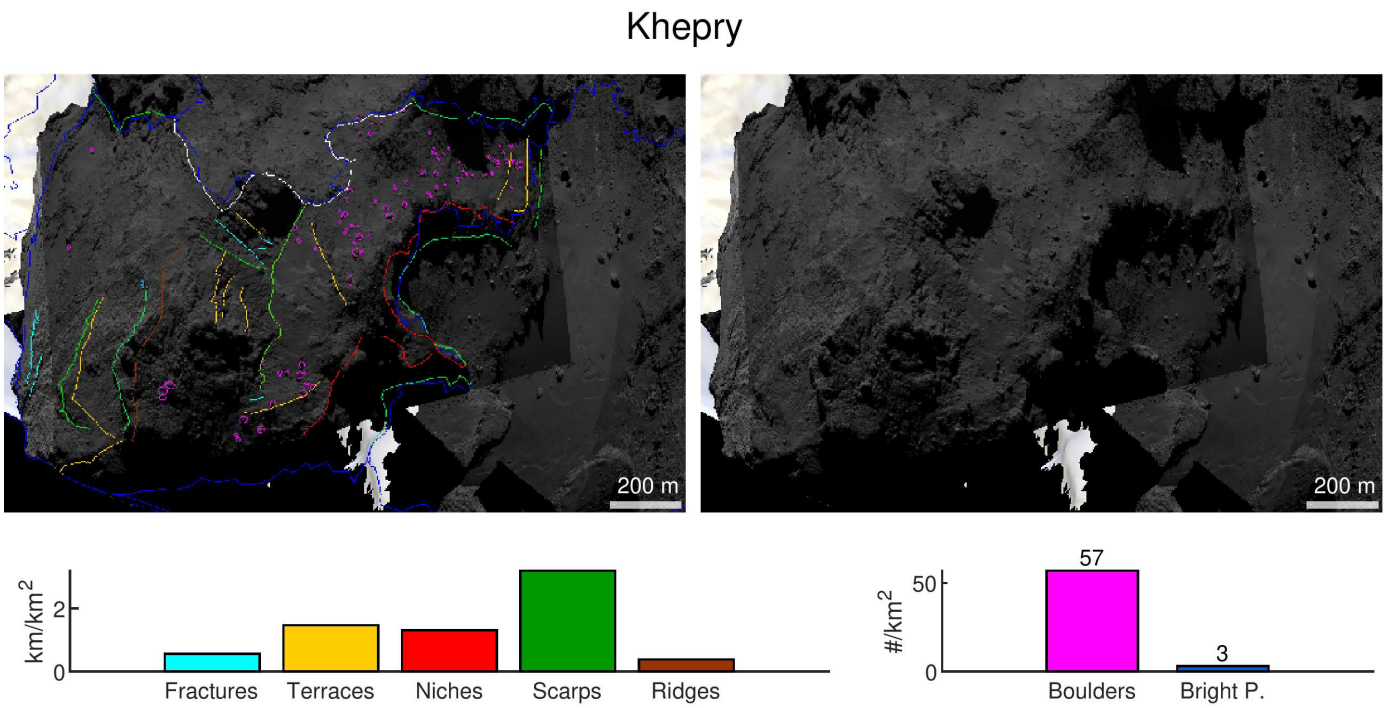

Fig. B.15. Identification of features in the Khepry region from images projected onto the SHAP4S shape model and annotated on the SBMT.